Icarus 457 (2026) 117166

Contents lists available at ScienceDirect

Icarus

journal homepage: www.elsevier.com/locate/icarus

Research Paper

Bottom control on heat transfer in thin spherical shells: Application to ice-covered ocean worlds

Filipe Terra-Nova [a,b,*], Hagay Amit [a], Gaël Choblet [a], Mathieu Bouffard [a], Gabriel Tobie [a], Ondřej Čadek [c]

[a] Nantes Université, Univ Angers, Le Mans Université, Laboratoire de Planétologie et Géosciences, CNRS UMR 6112, 2 rue de la Houssinière, F-44000 Nantes, France
[b] Université Paris Cité, Institut de physique du globe de Paris, CNRS, F-75005, Paris, France
[c] Charles University, Faculty of Mathematics and Physics, Department of Geophysics, V Holešovičkách 2, Prague 18000, Czech Republic

ARTICLE INFO

Keywords:
Jovian satellites
Hydrodynamical simulations
Saturnian satellites
Titan
Enceladus

ABSTRACT

The dynamical regime that prevails in sub-surface oceans of icy moons is thought to control the pattern of heat transfer in the oceans and possibly the topography of the ice layer above. However, if the heat flux across the seafloor is heterogeneous, its pattern may strongly affect the dynamics and the heat transfer in the ocean. Here we use numerical simulations of rotating convection in a thin spherical shell to explore the potential impact of heterogeneous inner boundary heat flux on the fluid dynamics and heat transfer in the thin liquid layer of icy moons. We prescribed synthetic large-scale heat flux patterns on the inner boundary corresponding to either polar or equatorial heating. Our results indicate that large-scale heating heterogeneity at the bottom of the ocean can strongly control the convection and heat transfer patterns in thin spherical shells, even for mild levels of heterogeneity amplitude. In practice, this means that an inner boundary heterogeneity can force polar or equatorial cooling at the top of the ocean, regardless of the ocean dynamics with homogeneous inner boundary conditions. Consequently, observed topographies at the surfaces of icy moons might not be deterministic of the competition between rotation and inertia in the sub-surface oceans and may provide constraints on large-scale heat flux anomalies emanating from the seafloor.

1. Introduction

Several icy moons contain liquid water oceans under a surface ice layer (e.g. Nimmo and Pappalardo, 2016). Global shape models and topography maps indicate lateral variation in ice shell thicknesses, notably on Europa, Enceladus and Titan (e.g. Nimmo et al., 2007). While these are possibly explained by laterally heterogeneous heat flux at the bottom of the ice shell (e.g. Kvorka et al., 2018; Čadek et al., 2019), this origin is still a matter of debate (Hemingway and Mittal, 2019; Čadek et al., 2019; Kang et al., 2022b; Kihoulou et al., 2023; Kvorka and Čadek, 2024; Bouffard et al., 2025; Gastine and Favier, 2025). One possibility explored by several previous studies is that competition between rotation and inertia in the ocean determines the latitudinal distribution of heat flux at the top of the ocean (Soderlund et al., 2014; Soderlund, 2019; Amit et al., 2020; Kvorka and Čadek, 2022; Hartmann et al., 2024). Numerical simulations of thermal convection in a thin rotating spherical shell shed light on these competing effects. In a large parametric study, Gastine et al. (2016) explored simulations with a moderate spherical shell thickness of aspect ratio $r_i/r_o = 0.6$ (where r_i and r_o are the radii of the inner and outer boundary, respectively), i.e. much thinner than Earth's outer core ($r_i/r_o = 0.35$) but substantially thicker than sub-surface oceans of icy moons ($r_i/r_o = 0.78 - 0.96$) (Vance et al., 2018; Čadek et al., 2019). When rotation effects are dominant and the system is closer to a rapidly-rotating dynamical regime (Gastine et al., 2016), the heat flux at the top of the shell is stronger outside the tangent cylinder (TC, an imaginary cylinder coaxial with the moon's rotation axis and tangent to the inner boundary of the ocean's spherical shell at the equatorial plane, see e.g. Aurnou et al., 2003), a configuration often termed 'equatorial cooling'. Conversely, when inertial effects take over and the system is close to a non-rotating dynamical regime (Gastine et al., 2016), the heat flux at the top of the shell is stronger inside the TC, a configuration often termed 'polar cooling' (Heimpel and Evans, 2013; Amit et al., 2020; Kvorka and Čadek, 2022, 2024; Terra-Nova et al., 2023; Bouffard et al., 2025). Remarkably, only equatorial cooling can reach extreme levels of dominance (Amit et al., 2020; Gastine and Aurnou, 2023; Hartmann et al., 2024). Upon further increase in convection vigor the system

* Corresponding author at: Université Paris Cité, Institut de physique du globe de Paris, CNRS, F-75005, Paris, France.
E-mail address: terranova@ipgp.fr (F. Terra-Nova).

https://doi.org/10.1016/j.icarus.2026.117166
Received 14 October 2025; Received in revised form 5 May 2026; Accepted 11 May 2026
Available online 15 May 2026

eventually reaches the non-rotating regime (Gastine et al., 2016) in which the outer boundary heat flux is uniform (Amit et al., 2020; Hartmann et al., 2024; Gastine and Favier, 2025).

The dynamical regimes delimited by Gastine et al. (2016) rely on global properties. They argued that the regimes separation is based on $Ra_T E^{4/3}$ vs. E, where Ra_T is the fixed temperature difference Rayleigh number and E the Ekman number (see Section 2). However, in rotating systems, convection is distinctive inside vs. outside the TC (e.g. Aurnou et al., 2003). In Gastine and Aurnou (2023), upon increasing the convective vigor, in the first regime, right after convection onset, convection only develops outside the TC. The second dynamical regime is reached when convection exceeds a critical value, leading to convection inside the TC as well. In this regime, increasing convection vigor leads to faster increase in heat flux inside the TC than outside it. Finally, at very strong convection the heat flux inside and outside the TC become comparable (Gastine and Aurnou, 2023).

This latitudinal asymmetry motivates alternative diagnostics based on the lateral distribution of heat flux at the outer boundary (Amit et al., 2020; Kvorka and Čadek, 2022; Gastine and Aurnou, 2023; Hartmann et al., 2024). The search for an optimal diagnostic has led to scaling laws of the form $Ra_T E^{\beta}$, with $\beta = 3/2$ (Amit et al., 2020; Hartmann et al., 2024), 12/7 (Kvorka and Čadek, 2022) and 4/3 (Gastine and Aurnou, 2023). These different β values reflect different quantifications of the physical mechanisms controlling the transition between dynamical regimes i.e. how rotational effects progressively weaken as convective forcing increases. The corresponding latitudinal distribution of heat flux may be interpreted either as competition between rotation and inertial effects (Amit et al., 2020; Kvorka and Čadek, 2022; Hartmann et al., 2024), the transition to a non-rotating dynamical regime (Kvorka and Čadek, 2022) or as a reorganization of flow associated with penetration of the TC (Gastine and Aurnou, 2023).

A classical Rossby number might not capture the actual role of inertia (Olson and Christensen, 2006). Extrapolating the dynamics in rotating convection models to conditions at sub-surface oceans may be more appropriate using the spectral behavior of the kinetic energy (Cabanes et al., 2024) rather than relying on an effective Rossby number (e.g. Amit et al., 2020; Kvorka and Čadek, 2022). Cabanes et al. (2024) applied the zonostrophic theory (Sukoriansky et al., 2002) to a set of rotating convection simulations at more rapid rotation and more vigorous convection conditions compared to previous studies. In their models, alternating east–west jets spontaneously form. Cabanes et al. (2024) predicted the strength of such zonal jets at sub-surface oceans of icy moons. Their approach captures the geostrophic component of the zonal flow outside the TC. However, the zonostrophic theory is based on laminar Ekman boundary layers whereas the models of Cabanes et al. (2024) are turbulent hence they likely overestimate jet speeds and the efficiency of heat transport towards the ice. In contrast, ocean circulation speeds based on global energy budgets suggest much weaker jets which are less capable of projecting heat from the bottom boundary to the top (Jansen et al., 2023).

Aside from the dynamical effects of rotation on convection, heterogeneous heat flux patterns at the top of the ocean may also result from heterogeneous boundary conditions at the ocean seafloor (Choblet et al., 2017a,b; Běhounková et al., 2021). Analogously, boundary heterogeneity at Earth's core-mantle boundary is thought to explain various geodynamo-related observations (for a review see e.g. Amit et al., 2015). Here we investigate bottom control on heat transfer in rotating thin spherical shells with application to ice-covered ocean worlds using numerical simulations of thermal convection either under prescribed uniform or large-scale heterogeneous bottom boundary heat flux conditions. In the context of sub-surface oceans of icy moons, Terra-Nova et al. (2023) imposed a heterogeneous bottom boundary heat flux pattern that may represent convective conditions in the underlying mantles of Ganymede and Titan (Choblet et al., 2017b) on rotating convection simulations with a thin spherical shell. They found preferred longitudes of intense outer boundary heat flux which are highly correlated with longitudes of intense inner boundary heat flux. Bouffard et al. (2025) imposed a bottom boundary heat flux pattern from 3D hydrothermal core simulations of Enceladus (Choblet et al., 2017a) with very large amplitudes of bottom boundary heterogeneity. Their model explains the enhanced hydrothermal activity and the thinning of Enceladus' crust below its south pole. Overall, it is of interest to explore how these two effects, i.e. rotating convection dynamics and bottom boundary heterogeneity, act together. In particular, can boundary heterogeneity reverse the cooling pattern of the ocean under homogeneous seafloor conditions?

This question has been addressed by Lemasquerier et al. (2023) in the context of Europa's sub-surface ocean (though they noted that implications for Ganymede and Titan are possible). In their ocean dynamics model, they imposed a heterogeneous seafloor heat flux pattern inferred from tidally-heated solid-state convection simulations of the silicate mantle below Europa's ocean (Běhounková et al., 2021). Lemasquerier et al. (2023) showed that polar heating from below leads to polar cooling at the top, i.e. the ocean is simply transmitting the heat flux boundary heterogeneity from top to bottom. They further found that this boundary control prevails regardless of the background convection/rotation state of the system.

Here we address the same question, i.e. whether internal dynamics or boundary control govern the pattern of heat transfer in sub-surface oceans, in a broader context that may apply to various icy moons. We impose both polar heating and equatorial heating patterns as bottom boundary conditions on our thermal convection numerical simulations in a thin rotating spherical shell, since both scenarios may in principle apply for various icy moons. We select reference homogeneous bottom heat flux models characterized by marked equatorial and polar cooling within our runs to test whether the boundary heterogeneity can overcome the underlying latitudinal heat flux pattern at the top of the ocean in extreme scenarios. As in Lemasquerier et al. (2023), we explore the dependence of the top cooling pattern on the amplitude of the bottom boundary heat flux heterogeneity. However, our study differs from that of Lemasquerier et al. (2023) in the following main aspects: (1) In addition to polar heating we also explore equatorial heating; (2) Our large-scale synthetic heating patterns may represent extreme heterogeneity scenarios at seafloors of various icy moons whereas Lemasquerier et al. (2023) focused on the case of Europa; (3) Our reference homogeneous bottom boundary heat flux models are selected to have peak equatorial cooling and nearly peak polar cooling at the ocean-ice upper interface in order to test whether the boundary heterogeneity can overcome extreme background dynamical states i.e. reference homogeneous cases with peak equatorial or polar cooling.

The paper is outlined as follows. In Section 2 we describe the numerical simulations including the heterogeneous bottom boundary conditions and we define measures of outer boundary heat flux cooling patterns. The results are presented in Section 3. In Section 4 we discuss missing ingredients in our models and the expected parameter values for ocean worlds. In Section 5 we summarize our main findings and speculate on the expected heat flux patterns in various sub-surface oceans of icy moons.

2. Methods

In Section 2.1 we present our hydrodynamical model formulation, our choice of control parameters, the spatial and temporal resolution and the numerical methods used. We present the general output diagnostics and focus on how we infer quantitatively the competition between polar and equatorial cooling at the ocean ceiling in Section 2.2.

2.1. Hydrodynamical models

We model thermal convection in a 3D rotating spherical shell by solving the set of hydrodynamics equations for the conservation of

Table 1
Inputs and outputs for models with homogeneous inner boundary heat flux.

Name	E	Ra_q	ℓ_{max}	$\widetilde{Ra}_{eff}$	Ro_{eff}	Nu	q_o^*	$q_o^{h/l}$	$\left(q_o^{h/l}\right)_{\theta 10}$	$\left(q_o^{h/l}\right)_{\theta 5}$	τ_u
$\mathcal{A}$	1e−04	5e+06	256	13.34	2.87	2.140	0.23	−0.043	−0.094	−0.098	434
$\mathcal{B}$	1e−04	1e+07	256	17.38	3.75	3.284	0.21	−0.025	−0.043	−0.051	449
$\mathcal{C}$	1e−04	4e+07	256	32.23	6.94	7.086	0.23	0.041	0.040	0.029	474
$\mathcal{D}$	1e−04	8e+07	288	47.75	10.29	9.565	0.20	0.040	0.035	0.025	115
$\mathcal{E}$	1e−04	2e+08	288	87.52	18.86	13.046	0.18	0.041	0.059	0.051	381
$\mathcal{F}$	1e−04	3e+08	427	115.59	24.90	14.817	0.17	0.056	0.079	0.070	253
$\mathcal{G}$	1e−04	4e+08	427	141.37	30.46	16.154	0.18	0.056	0.084	0.080	224
$\mathcal{H}$	1e−04	7e+08	427	209.50	45.14	19.076	0.17	0.056	0.093	0.089	132
$\mathcal{I}$	1e−04	1e+09	512	270.79	58.34	21.083	0.17	0.053	0.100	0.099	218
$\mathcal{J}$	1e−04	4e+09	512	721.72	155.49	31.642	0.14	0.031	0.076	0.073	122
$\mathcal{K}$	5e−05	5e+05	288	1.13	0.22	1.000	0.01	0.004	0.001	−0.006	350
$\mathcal{L}$	5e−05	2e+06	288	4.01	0.77	1.131	0.09	−0.005	−0.034	−0.040	541
$\mathcal{M}$	5e−05	5e+06	288	8.23	1.58	1.376	0.22	−0.034	−0.087	−0.095	304
$\mathcal{N}$	5e−05	4e+07	427	20.37	3.91	4.449	0.22	−0.037	−0.068	−0.078	389

E is the Ekman number (4), Ra_q is the conventional flux-based Rayleigh number (6). In all cases $Pr = 1$. $\widetilde{Ra}_{eff}$ is the effective level of convective supercriticality (13) and Ro_{eff} is the effective Rossby number (14). ℓ_{max} is the spherical harmonic truncation degree and order. All simulations have 161 grid points in the radial direction, the number of grid points in the longitudinal and latitudinal directions n_ϕ and n_θ in our setup are related to ℓ_{max} by $n_\phi = 3\ell_{max}$ and $n_\theta = n_\phi/2$. τ_u is the duration of the simulation in units of advection times D/U, where D is the shell thickness and U the RMS velocity amplitude in the shell computed based on the total kinetic energy $U = \sqrt{2E_{kin}}$. q_o^* denotes the amplitude of resulting outer boundary heat flux heterogeneity. The main model pattern outputs are the ratios of outer boundary heat flux at high/low latitudes $q_o^{h/l}$ (based on Amit et al., 2020), $\left(q_o^{h/l}\right)_{\theta 10}$ (based on Lemasquerier et al., 2023) and $\left(q_o^{h/l}\right)_{\theta 5}$ (based on Gastine and Aurnou, 2023). Cases $\mathcal{A}$ and $\mathcal{G}$ (denoted in bold) are used as reference cases for exploring the impact of a heterogeneous inner boundary heat flux.

momentum, energy and mass in the Boussinesq approximation. These write, in non-dimensional form,

$$E\left(\frac{\partial \mathbf{u}}{\partial t} + \mathbf{u}\cdot\nabla\mathbf{u} - \nabla^2\mathbf{u}\right) + 2\hat{z}\times\mathbf{u} + \nabla P = Ra_q^*\left(\frac{r_o}{\mathbf{r}}\right)^2 T, \tag{1}$$

$$\frac{\partial T}{\partial t} + \mathbf{u}\cdot\nabla T = \frac{1}{Pr}\nabla^2 T, \tag{2}$$

$$\nabla\cdot\mathbf{u} = 0, \tag{3}$$

where $\mathbf{u}$ is the fluid velocity, $\hat{z}$ the direction of the rotation axis, P the pressure, $\mathbf{r}$ the radial position vector, r_o the outer boundary radius and T the temperature. We use an inversely squared radial gravity profile $g = g_o\left(\frac{r_o}{r}\right)^2$ in the buoyancy force in (1) as in e.g. Kang et al. (2022b) which is the relevant radial dependence for relatively light outer envelopes as sub-surface oceans of icy moons i.e. corresponding to a centrally-condensed mass (Gastine et al., 2015).

Eqs. (1)–(2) are governed by three (internal) control parameters. The Ekman number represents the ratio of viscous to Coriolis forces:

$$E = \frac{\nu}{\Omega D^2}. \tag{4}$$

The Prandtl number is a ratio of diffusivities:

$$Pr = \frac{\nu}{\kappa}. \tag{5}$$

The modified Rayleigh number Ra_q^* represents the ratio of buoyancy vs. retarding effects. It is related to the conventional Rayleigh number Ra_q by $Ra_q^* = Ra_q E Pr^{-1}$, where the conventional heat flux based Rayleigh number is given by

$$Ra_q = \frac{\alpha g_o q_0 D^4}{\kappa\nu k}. \tag{6}$$

In (4)–(6), Ω is the rotation rate, ν the kinematic viscosity, D the shell thickness, g_o the gravitational acceleration at the outer boundary, q_0 the mean inner boundary heat flux, k the thermal conductivity and κ the thermal diffusivity. Models output time is given in units of viscous diffusion time D^2/ν. All simulations were run using the pseudo spectral MagIC code (Wicht, 2002, https://github.com/magic-sph/magic) for fluid dynamics in a spherical shell coupled with efficient spherical harmonic transforms (Schaeffer, 2013).

In all simulations the inner to outer boundary radii ratio is set to 0.8, corresponding to a relatively thin shell compared e.g. to Earth's outer core aspect ratio of 0.35 (e.g. Dziewonski and Anderson, 1981) and within the range (though at its lower edge) of most aspect ratio estimates of 0.78–0.96 for the subsurface oceans of several icy moons (Jara-Orué and Vermeersen, 2016; Vance et al., 2018; Čadek et al., 2019). Two types of simulations are explored. First, we study models with a uniform bottom boundary heat flux with the goal of revealing the difference between fixed temperature to fixed flux condition on the dynamics, in particular the heat transfer latitudinal dependence (Table 1). Second, for two of these reference cases ($\mathcal{A}$ and $\mathcal{G}$ in Table 1, corresponding respectively to equatorial and polar heating at the ocean-ice interface) we impose single harmonic heat flux patterns $-Y_2^0$ and $+Y_2^0$ at the inner boundary which correspond to equatorial and polar heating, respectively (see Table 2). Our choice of $\pm Y_2^0$ patterns was inspired by studies of core dynamics with heterogeneous core-mantle boundary heat flux where such patterns are known to have a profound impact on the magnetohydrodynamics (e.g. Glatzmaier et al., 1999; Olson and Amit, 2014; Frasson et al., 2025). The objective here is to examine whether inner boundary equatorial or polar heating can inverse (or amplify) a background pattern of outer boundary equatorial or polar cooling (Amit et al., 2020). The amplitude of the inner boundary heat flux lateral heterogeneity is quantified by (Terra-Nova et al., 2023):

$$q_i^* = \frac{q_{max} - q_{min}}{2q_0}, \tag{7}$$

where q_{max} and q_{min} are the maximum and minimum of the inner boundary heat flux, respectively. Here, q_i^* (where i denotes inner boundary) is an additional control parameter of the simulations. The amplitude of this heat flux heterogeneity q_i^* is limited to moderate values (i.e. unity order of magnitude, see Table 2) in order to demonstrate that boundary control may emerge rather easily. Fixed temperature is set on the outer boundary (as in e.g. Lemasquerier et al., 2023), mimicking a constant melting temperature (although the phase change boundary is somewhat more complex, see e.g. Kvorka and Čadek, 2024). In practice, with fixed temperature condition the heat flux on the outer boundary is an output of the models, allowing to investigate the resulting cooling patterns. On both boundaries the mechanical boundary conditions are no-slip. We explore different combinations of control parameters (Table 1) aiming to span various cooling patterns.

2.2. Diagnostics

Global diagnostic parameters are reported in Table 1. Following Gastine and Aurnou (2023), we consider the level of convective supercriticality in rapidly rotating fluids $\widetilde{Ra}$ (e.g. Aurnou et al., 2020)

Table 2
Input and outputs of models with heterogeneous inner boundary heat flux.

Name	Pattern	q_i^*	$\widetilde{Ra}_{eff}$	Ro_{eff}	Nu	q_o^*	$q_i^{h/l}$	$q_o^{h/l}$	$\left(q_o^{h/l}\right)_{\theta 10}$	$\left(q_o^{h/l}\right)_{\theta 5}$	τ_u
$\mathcal{A}$	Y_0^0	0.00	10.84	2.34	2.14	0.23	0.000	−0.043	−0.094	−0.098	434
$\mathcal{A}_{e.2}$	$-Y_2^0$	0.74	9.22	1.99	2.52	0.81	−0.428	−0.430	−0.806	−0.822	411
$\mathcal{A}_{e.3}$	$-Y_2^0$	1.11	7.66	1.65	3.03	1.13	−0.676	−0.637	−1.201	−1.213	414
$\mathcal{A}_{e.4}$	$-Y_2^0$	1.47	5.99	1.29	3.87	1.41	−0.937	−0.837	−1.594	−1.597	410
$\mathcal{A}_{p.2}$	Y_2^0	0.74	10.73	2.31	2.16	0.73	0.364	0.300	0.504	0.514	477
$\mathcal{A}_{p.3}$	Y_2^0	1.11	10.51	2.26	2.21	1.16	0.530	0.466	0.731	0.747	596
$\mathcal{A}_{p.4}$	Y_2^0	1.47	10.19	2.19	2.28	1.55	0.678	0.610	0.893	0.908	552
$\mathcal{G}$	Y_0^0	0.00	114.93	24.76	16.15	0.18	0.000	0.056	0.084	0.080	224
$\mathcal{G}_{e.1}$	$-Y_2^0$	0.37	114.04	24.57	16.28	0.28	−0.204	−0.112	−0.259	−0.274	226
$\mathcal{G}_{e.2}$	$-Y_2^0$	0.74	111.24	23.97	16.69	0.63	−0.426	−0.276	−0.759	−0.801	220
$\mathcal{G}_{e.3}$	$-Y_2^0$	1.11	86.01	18.53	21.59	0.73	−0.673	−0.405	−0.902	−0.914	221
$\mathcal{G}_{e.4}$	$-Y_2^0$	1.47	40.37	8.70	45.99	0.78	−0.931	−0.474	−0.920	−0.925	187
$\mathcal{G}_{p.1}$	Y_2^0	0.37	113.63	24.48	16.34	0.48	0.189	0.208	0.333	0.334	257
$\mathcal{G}_{p.2}$	Y_2^0	0.74	110.65	23.84	16.78	0.77	0.364	0.350	0.535	0.540	264
$\mathcal{G}_{p.3}$	Y_2^0	1.11	105.29	22.68	17.63	1.09	0.531	0.478	0.710	0.720	258
$\mathcal{G}_{p.4}$	Y_2^0	1.47	97.26	20.95	19.09	1.36	0.680	0.576	0.851	0.867	221

Cases $\mathcal{A}$ and $\mathcal{G}$ correspond to the same cases as in Table 1. The patterns correspond to single harmonics. q_i^* is the amplitude of the imposed inner boundary heat flux heterogeneity. Subscripts e/p denote equatorial/polar heating patterns of imposed inner boundary heat flux heterogeneity. Subscripts .x denote specific amplitudes of imposed inner boundary heat flux heterogeneity.

as an effective measure of the competition between convective and rotational effects

$$\widetilde{Ra} = Ra_T E^{4/3}. \tag{8}$$

Note that (8) is given in terms of a Rayleigh number based on a fixed temperature difference between the bottom and top boundaries Ra_T. In order to calculate an equivalent expression for fixed flux conditions, we relate Ra_T with our flux based Rayleigh number Ra_q by

$$Ra_T = \frac{Ra_q}{Nu}, \tag{9}$$

where Nu is the Nusselt number

$$Nu = \frac{\eta q_0 D}{k \Delta T}, \tag{10}$$

where $\eta = r_i/r_o$ and r_i is the inner boundary radius. Eq. (8) can then be expressed in terms of Ra_q as

$$\widetilde{Ra} = Ra_q E^{4/3} Nu^{-1}. \tag{11}$$

Because Ra_q is defined for constant gravitational acceleration g_0, to compare models with different gravity profiles Ra_q must be corrected to an effective Rayleigh number Ra_{eff}. Following Hartmann et al. (2024), for any gravity profile $g(r) = g_o(r/r_o)^\gamma$, the effective Rayleigh number depends on the power γ and the aspect ratio η as follows:

$$Ra_{eff} = \begin{cases} Ra_T \left(\frac{3\eta}{1+\eta+\eta^2+\eta^3}\right) & : \gamma = 1, \\ Ra_T & : \gamma = 0, \\ Ra_T \left(\frac{3}{1+\eta+\eta^2}\right) & : \gamma = -2, \end{cases} \tag{12}$$

for more details see the supplementary material of Hartmann et al. (2024). In our models $\gamma = -2$. However, for comparison with results from other studies we also use the other expressions in (12). The actual mean shell thickness of non-monophasic models from Gastine and Favier (2025) that we will compare to our results demand also the correction of E to an effective Ekman number $E_{eff} = E/h_L^2$ where h_L is the thickness of the liquid phase. In our models $h_L = 1$ hence simply $E = E_{eff}$. Finally, we define an effective level of convection supercriticality:

$$\widetilde{Ra}_{eff} = Ra_{eff} E_{eff}^{4/3} \tag{13}$$

and we evaluate the latitudinal dependence of heat transport in this study by an effective Rossby number that reflects the competition between convection and rotation effects (Hartmann et al., 2024):

$$Ro_{eff} = Ra_{eff} E_{eff}^{3/2}. \tag{14}$$

Next we introduce parameters that characterize the pattern of outer boundary cooling. To assess whether polar or equatorial cooling governs, we follow Amit et al. (2020) and calculate the ratio between the integrated heat flux inside and outside the tangent cylinder (TC) at the outer boundary $q_o^{h/l}$ (where 'h' and 'l' superscripts stand for high and low latitudes respectively). The co-latitude where the tangent cylinder (Aurnou et al., 2003) intersects the outer boundary θ_{tc} is given by $\sin\theta_{tc} = r_i/r_o$. For $r_i/r_o = 0.8$, the TC co-latitude is $\theta_{tc} \approx 53°$. The integrated heat flux inside the TC is given by

$$q_o^h = \frac{1}{S^h}\left(\int_0^{2\pi}\int_0^{\theta_{tc}} q_o dS + \int_0^{2\pi}\int_{\pi-\theta_{tc}}^{\pi} q_o dS\right) \tag{15}$$

and outside the TC by

$$q_o^l = \frac{1}{S^l}\int_0^{2\pi}\int_{\theta_{tc}}^{\pi-\theta_{tc}} q_o dS, \tag{16}$$

where S^h and S^l denote the outer boundary spherical surface areas inside and outside the TC, respectively, and $dS = r_o^2 \sin\theta d\phi d\theta$ is a surface increment with ϕ and θ being longitude and co-latitude, respectively. Polar vs. equatorial cooling is defined by

$$q_o^{h/l} = \frac{q_o^h - q_o^l}{q_o^h + q_o^l}. \tag{17}$$

Note that here we use the full outer boundary heat flux q_o, not its anomaly δq_o, to avoid division by zero. Also note that each integral is normalized by the appropriate area so we do not calculate total fluxes but mean fluxes (or flux density). The expression (17) gives positive/negative $q_o^{h/l}$ values for polar/equatorial cooling, respectively. In addition, we consider alternative regional measures of the high to low latitudes ratio of outer boundary heat flux based on (17). Lemasquerier et al. (2023) defined a regional polar vs. equatorial cooling, which we term $\left(q_o^{h/l}\right)_{\theta 10}$, by considering q_o^h as the mean value inside regions delimited by a 10° cap around the poles and q_o^l as the mean value inside a region delimited by ±10° around the geographic equator. Similarly, Gastine and Aurnou (2023) defined a stricter regional measure using 5° to delimit polar and equatorial regions, which we term $\left(q_o^{h/l}\right)_{\theta 5}$, in order to quantify latitudinal regionalization of Nu.

Next, we evaluate the amplitude of resulting outer boundary heat flux heterogeneity. We use a similar expression to that applied to

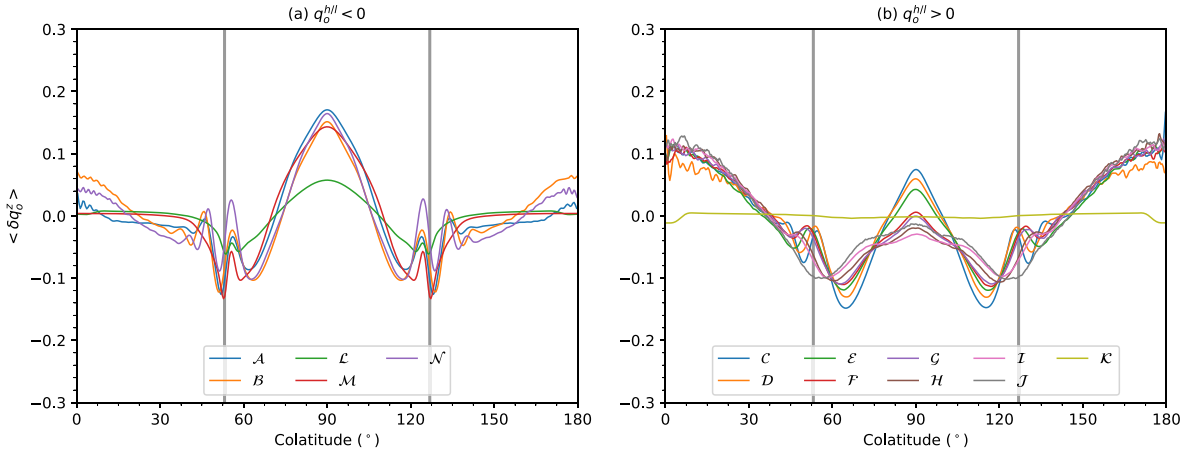

Fig. 1. Outer boundary heat flux anomaly $\langle \delta q_o^z \rangle$ averaged along latitude lines and normalized by q_0 vs. co-latitude for the models with homogeneous inner boundary heat flux. Solid vertical gray lines denote the tangent cylinder limits. Equatorial and polar cooling cases are shown in (a) and (b), respectively. (For interpretation of the references to color in the figure legends of this manuscript, the reader is referred to the web version of this article.).

imposed inner boundary heterogeneity (7) but using zonal averages:

$$q_o^* = \frac{q_{max}^z - q_{min}^z}{2\overline{q_o}}, \tag{18}$$

In (18), the superscripts z denote maximum and minimum values of the zonal averaged outer boundary heat flux defined by $q_o^z = \frac{1}{2\pi r_o \sin\theta} \int q_o d\phi$ and $\overline{q_o}$ is the mean outer boundary heat flux. Here the zonal average is considered in order to avoid longitudinal variability biases that may appear in the time averages due to the finite simulation time (Amit et al., 2020).

3. Results

3.1. Cooling patterns

First we consider the impact of fixed flux vs. fixed temperature at the bottom boundary on the resulting cooling pattern. Fig. 1 presents the outer boundary heat flux anomaly averaged along latitude lines vs. co-latitude for the models with homogeneous inner boundary heat flux. Fig. 1a shows the cases with negative $q_o^{h/l}$, i.e. with dominant equatorial cooling. Those are characterized by an equatorial heat flux peak, minima close to the intersections of the TC with the outer boundary and intermediate values near the poles. The patterns in Fig. 1a are more complex than the single peaked equatorial cooling distributions seen in the fixed bottom temperature models of Amit et al. (2020) and Kvorka and Čadek (2022). Indeed, cancellations due to mixed trends, i.e. positive anomalies both at the equator and at the poles, prevent larger absolute values of $q_o^{h/l}$. However, the equatorial peak is far larger than the polar and clearly dominates the latitudinal distribution of outer boundary heat flux in Fig. 1a. Polar cooling patterns are shown in Fig. 1b. Here, the largest heat flux is in the polar regions, but a local peak is also found at the equatorial region for all models. Again, cancellations due to mixed trends give relatively low values of $q_o^{h/l}$. Finally, the flat top heat flux distribution of case $\mathcal{K}$ is simply because this model approaches the conductive regime.

Fig. 2 summarizes the ratio between the outer boundary heat flux inside vs. outside the TC $q_o^{h/l}$(17) based on three different inner boundary thermal conditions. The gray circles correspond to fixed homogeneous heat flux (this study, Table 1). The green stars correspond to fixed heterogeneous heat flux (Terra-Nova et al., 2023) with a pattern taken from a solid convection model of the high pressure ice layer below the ocean (Choblet et al., 2017b). All other symbols correspond to fixed temperature (Amit et al., 2020; Kvorka and Čadek, 2022; Hartmann et al., 2024; Gastine and Favier, 2025). In general, the competition between inertial and rotation effects controls the pattern of outer boundary heat flux (Amit et al., 2020; Kvorka and Čadek, 2022). Stronger rotation effects lead to equatorial cooling, whereas stronger inertial effects lead to polar cooling. However, the magnitude of the equatorial vs. polar cooling ratio is substantially larger with fixed bottom temperature than with fixed bottom heat flux (homogeneous or small-scale heterogeneous), especially for models characterized by equatorial cooling, simply because with a fixed bottom temperature the outer boundary heat flux is free to vary laterally whereas with a fixed bottom flux in a thin shell the outer boundary heat flux is more constrained by the imposed bottom boundary heat flux. Indeed, in our models with homogeneous bottom boundary heat flux we found that the values of the high- and low-latitudes Nusselt numbers are not very different (as opposed to the findings of e.g. Gastine and Aurnou, 2023, with fixed temperature bottom boundary condition), leading to a very modest range of $q_o^{h/l}$ values, in agreement with the small-scale heterogeneous bottom boundary heat flux models of Terra-Nova et al. (2023), despite exploring a set of models covering ~3 orders of magnitude of Ro_{eff} values.

We note that in a set-up that is comparable to ours in principle (i.e. prescribing a uniform flux), Bire et al. (2022) obtain a similar behavior but reach significantly larger value for $q_o^{h/l}$ (between −0.2 and 0.25). Their simulations span much wider ranges for Ra, E and quite distinct aspect ratios are also considered. In their simulations, the maximum values of $q_o^{h/l}$ are nevertheless observed for parameters comparable to those used in the present study. Deviations would thus have to be attributed either to distinct modeling choices used in their study: a free-slip top, a uniform gravity or the simplified treatment of sphericity. Whatever the origin of this discrepancy, observed values of $q_o^{h/l}$ for a prescribed bottom flux never reach the strong equatorial cooling (up to 0.6) obtained with a fixed bottom temperature. Strong polar cooling ($q_o^{h/l} > 0.2$) is not found for any bottom boundary heat flux pattern (Fig. 2), unlike models with fixed temperature conditions that reach larger positive $q_o^{h/l}$ values. Overall, imposing either homogeneous or small-scale heterogeneous bottom heat flux boundary condition prevents strong latitudinal regionalization of heat transfer.

Comparison among the various models in Fig. 2 shows that the local maxima of $q_o^{h/l}$, associated with peak polar cooling, span a much wider range of Ro_{eff} values than the minima associated with equatorial cooling (see wide blue vs. narrow yellow hatched areas in Fig. 2). Indeed, the onset of polar convection (Gastine and Aurnou, 2023), which coincides with peak equatorial cooling in Fig. 2, appears broadly consistent across studies. However, the balance between rotational and inertial effects at which polar convection ceases to intensify more

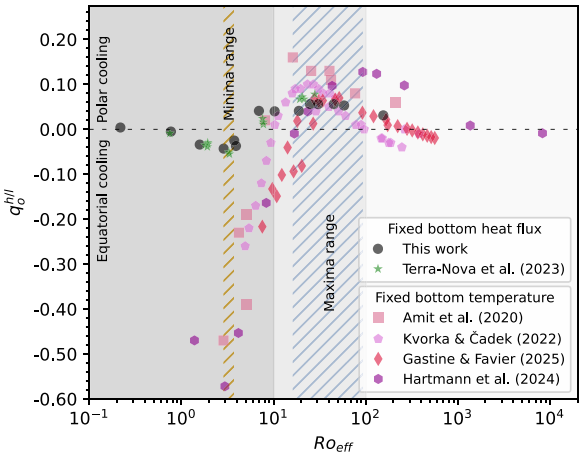

Fig. 2. $q_o^{h/l}$ vs. Ro_{eff} for models with fixed bottom temperature and fixed bottom heat flux (see legend). Background colors correspond to the expected latitudinal regionalization of heat flux (Gastine and Favier, 2025): $Ro_{eff} \leq 10$ (gray) corresponds to equatorial cooling, $10 \leq Ro_{eff} \leq 100$ (light gray) to polar cooling and $Ro_{eff} \geq 100$ (lighter gray) to uniform cooling. Yellow and blue hatched areas correspond to ranges of minima and maxima of $q_o^{h/l}$, respectively, obtained by the various studies listed in the legend.

rapidly than equatorial convection (Gastine and Aurnou, 2023) varies substantially among models.

The latitudinal dependence of the outer boundary heat flux in our fixed bottom heat flux models exhibits transitions at the Ro_{eff} values proposed by Gastine and Favier (2025). As seen in Fig. 2, equatorial cooling tends to occur for $Ro_{eff} < 10$ while polar cooling is reached when $10 < Ro_{eff} < 100$. For $Ro_{eff} > 100$ the outer boundary heat flux decreases as expected on approach to the non-rotating regime, while for $Ro_{eff} \ll 1$ (case $\mathcal{K}$) the heat flux is uniform because the system is in the conductive regime (Gastine et al., 2016).

To verify the robustness of the results in Fig. 2, we investigate whether the values of polar vs. equatorial cooling are related to the specific definition of $q_o^{h/l}$ (Table 1). In order to do that, we compare the $q_o^{h/l}$ values of our models obtained with the definition of Amit et al. (2020) with alternative measures of polar cooling vs. equatorial cooling based on two regional quantifications $\left(q_o^{h/l}\right)_{\theta 10}$ and $\left(q_o^{h/l}\right)_{\theta 5}$ which correspond to polar caps and equatorial regions delimited by 10° and 5° (Lemasquerier et al., 2023; Gastine and Aurnou, 2023, see Section 2.2 and Fig. 3 for schematic illustration).

The two regional quantifications give somewhat larger magnitudes (Fig. 4). This is consistent with equatorial and polar peaks (Fig. 1), i.e. restricting the measures to around the peaks gives larger values. However, qualitatively the results are unchanged, with stronger rotation effects leading to equatorial cooling while stronger convection effects lead to polar cooling for all three quantifications (Fig. 4). From hereafter we focus on the quantification of Amit et al. (2020) based on the TC limits and accounting for the entire outer boundary surface.

We then imposed two single harmonic inner boundary heat flux heterogeneities. We chose the heating patterns Y_2^0 and $-Y_2^0$ because these patterns are most likely to have a strong impact on the latitudinal distribution of outer boundary cooling pattern. We compared models with various heterogeneity amplitudes q_i^* applied to two of our reference homogeneous simulations (Table 2). We selected one reference model with a relatively low level of convective supercriticality ($\widetilde{Ra} = 10.84$) that results in equatorial cooling (case $\mathcal{A}$ in Table 1) and another with a larger convective supercriticality ($\widetilde{Ra} = 114.93$) that gives polar cooling (case $\mathcal{G}$ in Table 1).

Fig. 5 presents the outer boundary heat flux anomaly averaged along latitude lines vs. co-latitude for our models with fixed single harmonic heterogeneous inner boundary heat flux patterns. All equatorial cooling models in Fig. 5a are characterized by a strong single peak equatorial heat flux (as in Amit et al., 2020; Kvorka and Čadek, 2022) regardless of the reference model used. Likewise, all polar cooling models in Fig. 5b have polar peaks and equatorial lows, which is found for only a few models in studies with homogeneous boundary conditions (Amit et al., 2020; Kvorka and Čadek, 2022). Larger q_i^* models yield more prominent (polar or equatorial) cooling patterns. Bottom equatorial heating superimposed on reference equatorial cooling cases produce significantly stronger equatorial cooling than when superimposed on reference polar cooling (compare dashed vs. solid in Fig. 5a). However, the resulting polar cooling latitudinal distributions of heat flux seem comparable for the two reference cases (compare dashed vs. solid in Fig. 5b). Finally, the signature of the TC is much less evident in the zonal averages in the models with heterogeneous heat flux (Fig. 5) than those with homogeneous heat flux (Fig. 1) because the imposed heterogeneous bottom heating amplifies top cooling heterogeneity thereby masking the TC signal.

The bottom polar heating Y_2^0 pattern results in top polar cooling, and likewise the bottom equatorial heating Y_2^0 pattern results in top equatorial cooling, as expected, regardless of the cooling pattern of the reference case and for all explored q_i^* values (Fig. 6) including those below unity that do not lead to any local stratification at the top of the shell. The lowest q_i^* models that reverse the cooling patterns have almost identical effective Rossby numbers (and hence almost identical Nusselt numbers) as their respect homogeneous cases (Fig. 6a top left and bottom right), hence these pattern reversals occur at comparable main convective vigor and are not due to shifts in dynamical regimes. The values of $q_o^{h/l}$ range from −0.837 to 0.610, a dramatically larger range than in our homogeneous models (Fig. 6; also compare Tables 1 and 2). Even with a very mild q_i^* (7) of 0.37, a Y_2^0 heating pattern enhances the resulting polar cooling by a factor of ∼3.7, while a $-Y_2^0$ heating pattern inverses the reference polar cooling case into equatorial cooling with an absolute $q_o^{h/l}$ value twice larger (Table 2 and Fig. 6a). Interestingly, increasing amplitudes of bottom boundary heterogeneity q_i^* with equatorial heating in the reference polar cooling cases leads to a noticeable decrease in the resulting Nusselt number Nu and hence in the effective Rossby number Ro_{eff} (Fig. 6a).

Stronger amplitude of imposed bottom heat flux heterogeneity gives strong equatorial or polar cooling, as expected. Fig. 6b testifies for an overall preservation of the imposed latitudinal distribution of heat flux at the outer boundary of the shell. For cases $\mathcal{A}$ (with a reference homogeneous case corresponding to equatorial cooling), both polar ($\mathcal{A}_{p,*}$) and equatorial ($\mathcal{A}_{e,*}$) heating, as well as for cases $\mathcal{G}$ (with a reference homogeneous case corresponding to polar cooling) with polar heating ($\mathcal{G}_{p,*}$), the latitudinal cooling distribution is comparable to the imposed latitudinal heating distribution — see slopes of nearly 1 for the dashed curve and for the solid curve with Y_2^0 in Fig. 6b. Nevertheless a somewhat lower slope is found for the reference polar cooling cases $\mathcal{G}$ with $-Y_2^0$ (see the solid curve in Fig. 6b). This difference can be simply explained by the larger impact of boundary heterogeneity on tracers (here temperature) distributions when the main convection vigor is weaker (as seen in cases $\mathcal{A}$) (Gubbins et al., 2007; Sreenivasan, 2009). However, it fails to explain the different slopes between cases $\mathcal{G}_{e,*}$ and $\mathcal{G}_{p,*}$ (or even, though less remarkable, between $\mathcal{A}_{e,*}$ and $\mathcal{A}_{p,*}$). Here, we will show that stratified layers forming regionally at the bottom of the ocean explain those lower slopes (see Section 3.2).

We also considered the alternative measures of $q_o^{h/l}$ in the context of heterogeneous bottom heat flux. Again the magnitudes of $\left(q_o^{h/l}\right)_{\theta 10}$ and $\left(q_o^{h/l}\right)_{\theta 5}$ surpass those of $q_o^{h/l}$. Interestingly, for the $\mathcal{A}_{e.3}$ and $\mathcal{A}_{e.4}$ models those alternative measures give magnitude values above unity (Table 2). This occurs because in these two models q_i^* is larger than unity, allowing not only heating but also local cooling of the sub-surface ocean by the heterogeneous inner boundary heat flux. Otherwise, the main result remains unchanged regardless of the polar vs. equatorial cooling quantification: prescribed bottom polar/equatorial

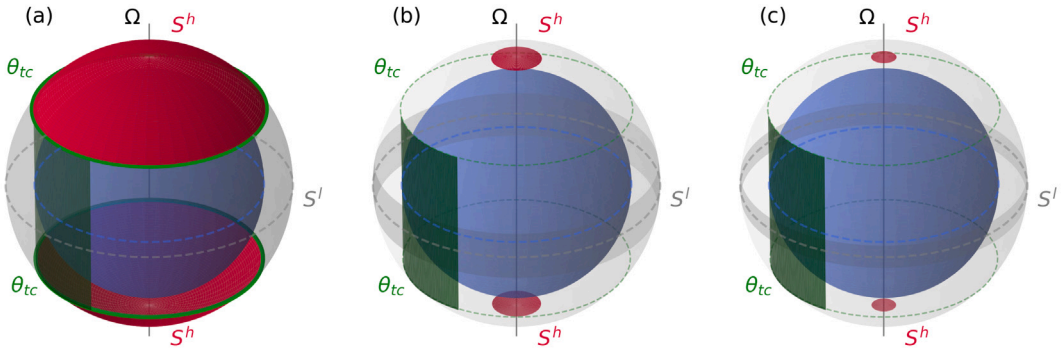

Fig. 3. Illustrations of the areas S_l (gray) and S_h (red) used for quantifying $q_o^{h/l}$, $\left(q_o^{h/l}\right)_{\theta 10}$ and $\left(q_o^{h/l}\right)_{\theta 5}$ as in (a) Amit et al. (2020), (b) Lemasquerier et al. (2023) and (c) Gastine and Aurnou (2023), respectively. The green surface denotes the edge of the tangent cylinder.

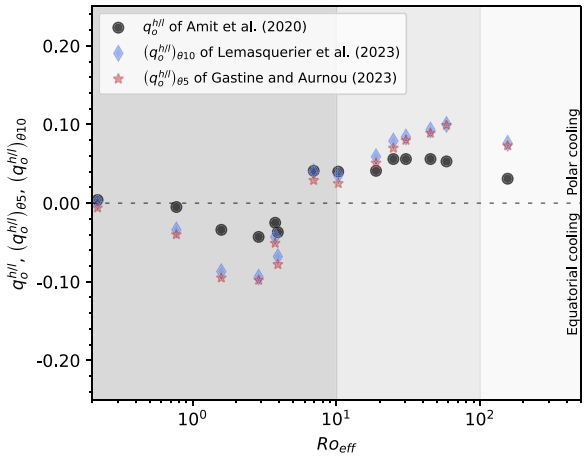

Fig. 4. $q_o^{h/l}$ based on three definitions of outer boundary heat flux regionalization from previous studies (see legend) vs. Ro_{eff} for our models with fixed bottom heat flux. As in Fig. 2, background colors correspond to the expected latitudinal regionalization of outer boundary heat flux (Gastine and Favier, 2025).

heating leads to top polar/equatorial cooling, respectively, for both reference cooling configurations considered, $\mathcal{A}$ and $\mathcal{G}$ (Table 2).

It is of particular interest to explore the models in which the boundary heterogeneity reverses the cooling pattern that was obtained by the reference homogeneous cases. Fig. 7 shows decent linear fits for these two scenarios. The interception of the linear fits with $q_o^{h/l} = 0$ indicates that for q_i^* as low as ≈ 0.1 the cooling pattern is expected to reverse.

Next we evaluated the global amplitude of outer boundary heat flux heterogeneity q_o^* based on Eq. (18). For our reference homogeneous inner boundary heat flux cases (Fig. 8a), we found small q_o^* values with uniform outer boundary heat flux in the conductive regime ($Ro_{eff} < 1.0$). Largest q_o^* values are found for $Ro_{eff} \approx 1 - 10$. For Ro_{eff} larger than $\approx$ 10, q_o^* decreases with increasing Ro_{eff}. Overall, without an inner boundary heterogeneity, we obtain rather small q_o^* values of less than 0.25. In contrast, when an inner boundary heat flux heterogeneity was incorporated (Fig. 8b), we obtained substantially larger q_o^* values of up to ~1.5. The resulting amplitude of outer boundary heat flux heterogeneity increases almost at the rate of increase of the imposed amplitude on the inner boundary (see nearly 1 slopes in Fig. 8b), except again for the $\mathcal{G}$ cases with equatorial heating ($\mathcal{G}_{e,*}$) where the resulting amplitude of outer boundary heat flux heterogeneity increases more slowly than the rate of increase of the imposed amplitude of inner boundary heterogeneity (see slope ~1/2 in Fig. 8b). We also plot models with fixed temperature (Amit et al., 2020) in Fig. 8. The fixed temperature condition allows to obtain large q_o^* values (Fig. 8a), as with $q_o^{h/l}$ (Fig. 2). When q_i^* is an outcome of the models (rather than imposed), the bottom to top amplification of the heat flux heterogeneity with fixed temperature is the same as in our models with large-scale heterogeneous bottom boundary heat flux (Fig. 8b).

3.2. Dynamical origin

The stronger reduction in convective supercriticality for models with reference polar cooling ($\mathcal{G}$ cases) and large heterogeneity amplitude of imposed inner boundary equatorial heating (Fig. 6a) can be understood by examining the radial temperature gradient $\frac{\partial T}{\partial r}$ as a function of depth r. The radial profiles in Fig. 9 are separated by $\mathcal{A}$ and $\mathcal{G}$ cases (Fig. 9 top and bottom respectively) and in the poles vs. the equator (Fig. 9 left and right respectively). Positive/negative values of $\partial T/\partial r$ denote stratified/unstable conditions respectively. With a large-scale boundary heterogeneous pattern, subadiabatic conditions may be reached when the amplitude of heterogeneity exceeds unity (e.g. Terra-Nova and Amit, 2024). Indeed, we found stratified layers forming regionally at the bottom of the ocean only for cases with $q_i^* > 1.0$. In addition, these stratified layers are found only for bottom equatorial heating and only inside the polar caps (dashed-dotted curves in Figs. 9a and c). Convection inside the tangent cylinder is more difficult to trigger (Gastine and Aurnou, 2023), hence it is there that stratification will first emerge (though with sufficiently large heterogeneity amplitude regional stratification may emerge at the equator as well, see e.g. Mound et al., 2019, in the context of Earth's core-mantle boundary). Subadiabatic conditions at the poles are induced by equatorial heating because with this pattern negative inner boundary heat flux anomalies prevail at the poles.

Because convection in cases $\mathcal{G}$ is stronger than in cases $\mathcal{A}$, the stratification for the latter cases takes place in the whole ocean inside the polar cap (Fig. 9a) whereas only the bottom half of the shell is stratified for cases $\mathcal{G}$ (Fig. 9c). Furthermore, the reference case $\mathcal{G}$ with homogeneous boundary conditions is characterized by polar cooling that is suppressed by the bottom equatorial heating, whereas the reference case $\mathcal{A}$ with homogeneous boundary conditions is characterized by equatorial cooling which is augmented by the imposed bottom equatorial heating. Therefore, the stronger reduction in convective supercriticality appears for the $\mathcal{G}$ models (Fig. 9a) due to the suppression of the polar cooling by the bottom equatorial heating.

Previous studies in the context of Earth's liquid outer core demonstrated that increasing q^* may produce relatively thin stratified layers near the heterogeneous boundary (e.g. Mound et al., 2019). In the case of thin sub-surface oceans, bottom boundary heterogeneity may lead to regional stratification formed from below which may extend radially to the top of the shell. This is indeed the case in our models with relatively weaker convection and large amplitude equatorial heating (Fig. 9a).

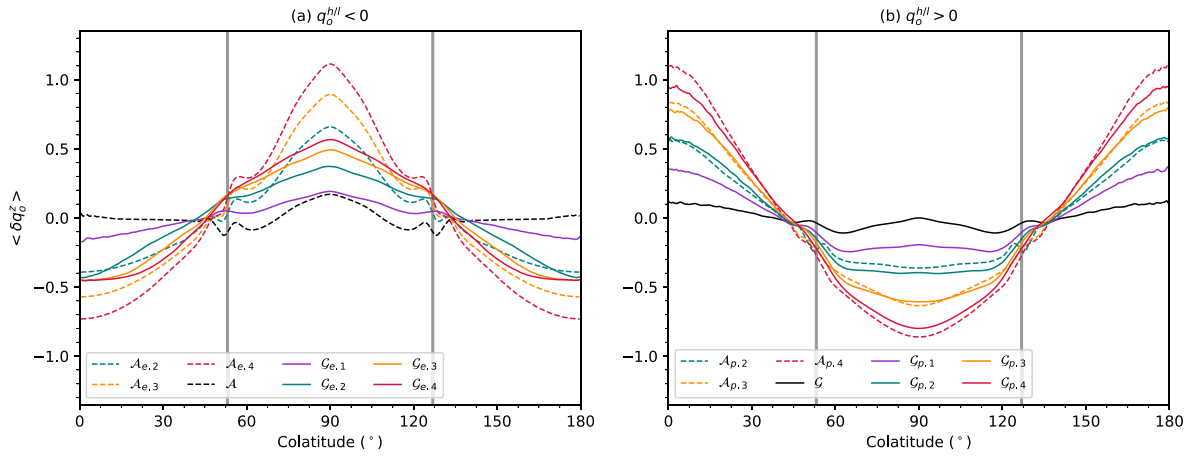

Fig. 5. Outer boundary heat flux anomaly averaged along latitude lines and normalized by q_0 vs. co-latitude for the models with heterogeneous inner boundary heat flux. Solid vertical gray lines denote the tangent cylinder limits. Equatorial and polar cooling cases are shown in (a) and (b), respectively. Dashed and solid curves correspond to $\mathcal{A}$ and $\mathcal{G}$ cases in which the reference models with homogeneous inner boundary heat flux are characterized by equatorial and polar cooling, respectively. Colors indicate different imposed inner boundary heat flux patterns and heterogeneity amplitudes (see legend and Table 2).

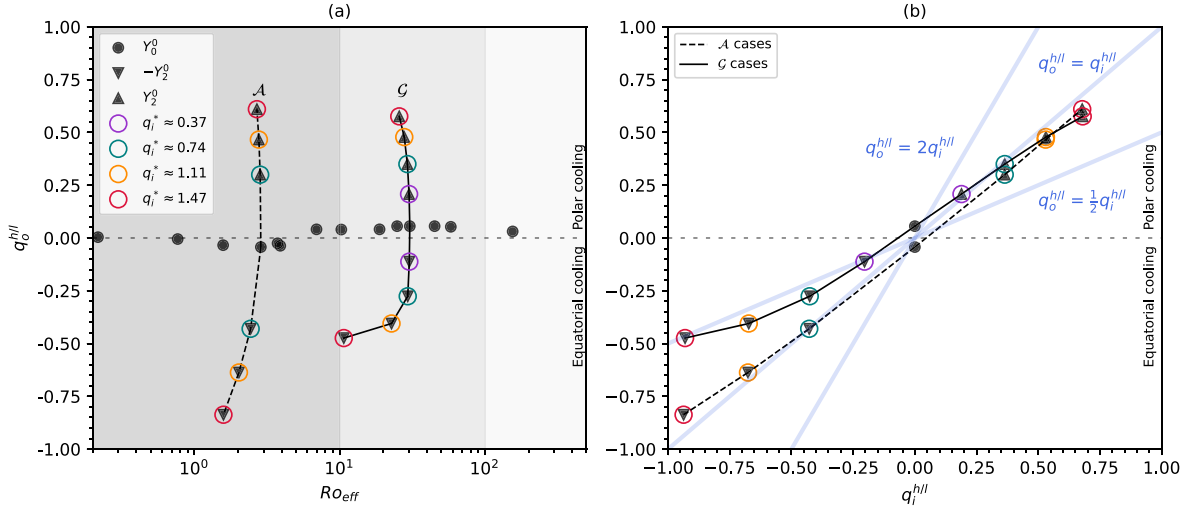

Fig. 6. $q_o^{h/l}$ vs. Ro_{eff} for all cases (a) and vs. $q_i^{h/l}$ for the heterogeneous inner boundary heat flux cases (b). Dashed and solid curves correspond to $\mathcal{A}$ and $\mathcal{G}$ cases in which the reference models with homogeneous inner boundary heat flux are characterized by equatorial and polar cooling, respectively. Background colors in (a) correspond to the expected latitudinal regionalization regimes of Gastine and Favier (2025), as in Fig. 2. Straight lines in (b) are given for reference of levels of amplification of the bottom boundary heterogeneity at the outer boundary.

The impact of the heterogeneous inner boundary heat flux on the dynamics in the shell is demonstrated using the models with the stronger heterogeneity amplitude q_i^* and their corresponding homogeneous cases for both low (Fig. 10) and high (Fig. 11) convective supercriticalities $\widetilde{Ra}$. We recall that the lower $\widetilde{Ra}$ reference case $\mathcal{A}$ corresponds to equatorial cooling, whereas the higher $\widetilde{Ra}$ reference case $\mathcal{G}$ corresponds to polar cooling. For each reference homogeneous case, models with imposed $-Y_2^0$ and $+Y_2^0$ patterns are compared. To interpret the latitudinal variability of the fluid dynamics and heat transfer, we focus on zonal temperature and velocity in the shell.

In Fig. 10, we explore models $\mathcal{A}$ which are characterized by relatively low $\widetilde{Ra}$ values of order ~10. The reference homogeneous bottom heat flux case (Fig. 10b) exhibits equatorial cooling. The flow outside the TC is organized in axial columns invariant in the direction of the rotation axis due to the dominance of rotation effects (e.g. Busse, 1975). The fluid inside the TC is warmer than outside the TC (Fig. 10b left). To elucidate the relations between the temperature and flow in the shell and the resulting outer boundary heat flux, consider the thermal wind equation (e.g. Pedlosky, 1987),

$$\frac{\partial u_\phi}{\partial z} \propto \frac{\partial T}{\partial \theta}. \tag{19}$$

Inside the TC the warmer poles (e.g. $\frac{\partial T}{\partial \theta} < 0$ inside the northern TC) induce a spiraling azimuthal shear flow pointing westward at the top of the shell and eastward at its bottom (Fig. 10b right), resembling the likely TC dynamics in Earth's liquid outer core (Olson and Aurnou, 1999; Livermore et al., 2017; Lézin et al., 2023). Outside the TC, at the equator, $\frac{\partial}{\partial z} \propto -\frac{\partial}{\partial \theta}$, hence the thermal wind equation further simplifies to $u_\phi \propto -T$ (see e.g. equation 7 of Christensen and Olson, 2003). In this reference equatorial cooling case $\mathcal{A}$, the cold equator yields eastward flow (Fig. 10b). In addition, the meridional circulation is invariant in the direction of the rotation axis and concentrated outside the TC (Fig. 10b).

When equatorial heating is imposed the temperature distribution inverses and colder fluid resides inside the TC (Fig. 10a left). Consequently, the zonal flow inside the TC also inverses, with eastward flow below at the top of the shell (Fig. 10a right). The moderate amplitude of bottom heat flux heterogeneity is insufficient to inverse the flow outside the TC. However, note that the eastward flow column slightly weakens whereas the higher latitude westward flow column strengthens with respect to the reference case (compare Fig. 10a and b right). In contrast, imposing polar heating reinforces the zonal temperature and

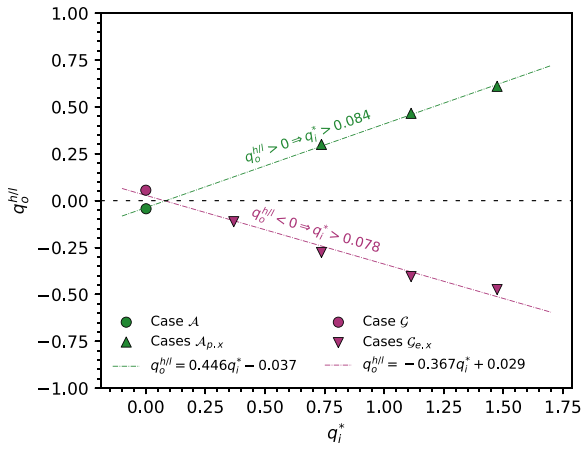

Fig. 7. $q_o^{h/l}$ vs. q_i^* for the cases in which the cooling pattern reverses compared to the respective homogeneous heat flux cases. Green and red solid curves are linear fits to $\mathcal{A}$ and $\mathcal{G}$ cases respectively. For interpretation of symbols see legend.

velocity trends of the reference equatorial cooling case. Warmer polar temperatures and westward polar vortices still prevail inside the TC (Fig. 10c). The effect is more pronounced outside the TC, where colder temperatures (Fig. 10c left) lead to a sweeping eastward flow and the meridional circulation diminishes there (Fig. 10c right).

The impact of the boundary heterogeneity is qualitatively similar for the models with the reference polar cooling case $\mathcal{G}$ which are characterized by higher $\widetilde{Ra}$ values of order ∼100 (Fig. 11). It is therefore worth focusing on the differences between the corresponding cases in Figs. 10 and 11. In the homogeneous bottom heat flux reference polar cooling case the temperature is more evenly distributed in latitude (Fig. 11b left) because the model, which as all our models resides in the transitional dynamical regime of Gastine et al. (2016), is closer to the non-rotating dynamical regime. Inside the TC the spiraling thermal wind signature vanished (Fig. 11b right), reflecting weaker rotational effects, though outside the TC invariant axial columns still prevail. In the equatorial heating model $\mathcal{G}_{e.4}$, the warmer fluid outside the TC yields a sweeping westward flow (Fig. 11a right), which is a much stronger dynamical response to the boundary heterogeneity compared to the gentler increase in westward flow in the corresponding case $\mathcal{A}_{e.4}$ (Fig. 10a right). In contrast, polar heating is less effective in terms of inversing flow trends in case $\mathcal{G}_{p.4}$ where the eastward time-average zonal flow does not fill the entire shell at the equator (Fig. 11c right) as opposed to the corresponding case $\mathcal{A}_{p.4}$ (Fig. 10c right). Nevertheless, the spiraling thermal wind inside the TC is re-established (Fig. 11c right).

Because in our models the heterogeneity is imposed at the seafloor by the envelope below the ocean, it is important to track the way convection varies across the ocean. In Fig. 12 we show the radial velocity at three different depths for models $\mathcal{A}$ with a reference homogeneous boundary condition characterized by equatorial cooling. When polar heating is imposed some weak convective activity outside the TC is observed at depth (Fig. 12i) but it vanishes at the top of the shell (Fig. 12c) resulting in strong polar cooling (Fig. 6). The weakening of convection outside the TC from bottom to top is more evident in models $\mathcal{G}$ with a reference homogeneous boundary condition characterized by polar cooling. When polar heating is imposed, comparable convective activity inside and outside the TC at depth (Fig. 13i) gradually fades with radial distance until reaching convection dominant inside the TC at the top of the shell (Fig. 13c). In the reference homogeneous case $\mathcal{G}$ the convection at depth is stronger at low latitudes (Fig. 13h) but becomes mixed at the top of the shell (Fig. 13b). Less radial variability is observed for the equatorial heating case (Figs. 13a, d and g). In summary, the dependence of the radial flow on depth shows the way the pattern imposed on the bottom boundary translates to the top of the shell. In all cases we find that convection outside the TC gets relatively weaker from bottom to top. This effect is more visible in the polar heating models (Figs. 12c, f, i and 13c, f, i).

Note that while the radial velocity amplitude is comparable in the homogeneous and heterogeneous $\mathcal{A}$ models (compare colorbar scales in Fig. 12), this is not the case for the $\mathcal{G}$ models in which the radial velocity amplitude is substantially larger for the homogeneous case (compare colorbar scales in Fig. 13). This is in contrast to the corresponding zonal flow amplitudes which are comparable (see colorbar scales in Fig. 11). This means that in these stronger mean convection $\mathcal{G}$ models a very large amplitude of lateral boundary heterogeneity substantially suppresses the main convection in the shell.

4. Implications for icy moons

Before entering the discussion on how the results obtained here for ocean dynamics may be understood in terms of spacecraft observations, we must stress that these simulations lack potentially important ingredients. The latter essentially relate to the possibility of stratification within the ocean as a result of variable salinity or of a negative thermal expansion coefficient (cf. e.g. Melosh et al., 2004; Ashkenazy and Tziperman, 2021; Bire et al., 2023; Ames et al., 2025). For low salinity, at low pressures, an inverse stratification is expected beneath the ice shell owing to a negative thermal expansion coefficient at temperatures close to the melting point. This probably applies to the case of Enceladus where the thickness of the stratification is under debate which bears key implications on vertical transport (Kang et al., 2022a; Bire et al., 2023; Zeng and Jansen, 2024). At higher salinities and/or higher pressures, stratification would be associated to melting of the ice, in particular above regions of elevated heat flux in case of a global equilibrium of the ice shell: this would result in local lenses of freshwater above the convecting ocean.

Even if the ocean is convecting throughout and prescribes a heterogeneous heat flux at the ice/ocean interface as described in the present study, regions of higher heat flux do not necessarily result in topographic lows. As demonstrated by Kihoulou et al. (2023), such surface manifestations in terms of relief require that the ice shell be conductive and that ice viscosity value be elevated. Latitudinal variations in surface temperature are also expected to affect the ice shell thickness: in the case of Ganymede, Kvorka et al. (2026) obtain a positive polar topography caused by a lower surface temperature in spite of a polar cooling regime for the ocean.

The model presented by Ashkenazy and Tziperman (2021) for Europa is archetypal in this regard as it precisely involves ingredients not included in our study (salinity, variations in surface temperature) while also prescribing a bottom ocean heat flux. Furthermore, a much smaller value of viscosity is considered in their study, a quite unique achievement in the previous literature. This model results in an overall agreement with the results obtained here (akin to the transitional polar cooling regime) with the addition of specific features (a weak stratification as well as transient Taylor columns). Again, Ashkenazy and Tziperman (2021) obtain a latitudinal profile for ice shell thickness variation that involves a thicker ice shell under the poles, probably as a consequence of colder surface temperature.

In addition, modeling the fluid dynamics and heat transfer in the sub-surface oceans may require proper coupling between the ocean and the solid ice crust above it, which are not accounted for in this present paper. Deviations from sphericity combined with the melting point dependence on pressure (Labrosse et al., 2018) may produce larger horizontal than radial thermal gradients leading to large-scale baroclinic flows in oceans of small moons (Kang, 2022; Zhang et al., 2024). Kang (2023) proposed that ice-ocean interface horizontal temperature gradients arising from melting are orders of magnitude larger

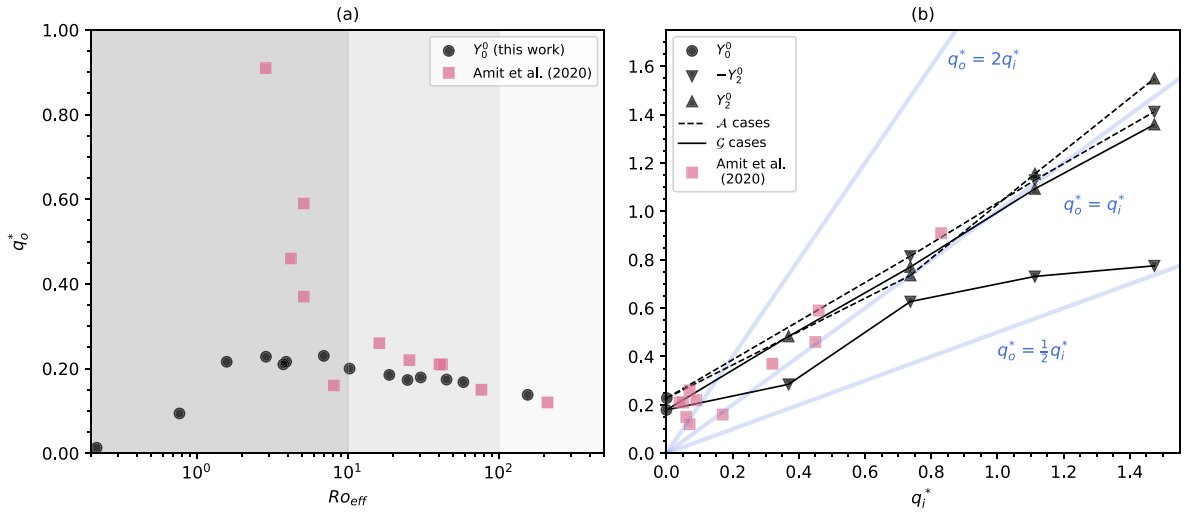

Fig. 8. Amplitude of outer boundary heat flux heterogeneity q_o^* vs. Ro_{eff} for the homogeneous inner boundary heat flux cases (a) and vs. q_i^* for the heterogeneous inner boundary heat flux cases (b). Dashed and solid curves in (b) correspond to $\mathcal{A}$ and $\mathcal{G}$ cases in which the reference models with homogeneous inner boundary heat flux are characterized by equatorial and polar cooling, respectively. Background colors in (a) correspond to the expected latitudinal regionalization regimes of Gastine and Favier (2025), as in Fig. 2. The results from Amit et al. (2020) are given for comparison. Note that in (b) q_i^* of Amit et al. (2020) is a result, unlike in our models where it is part of the setup.

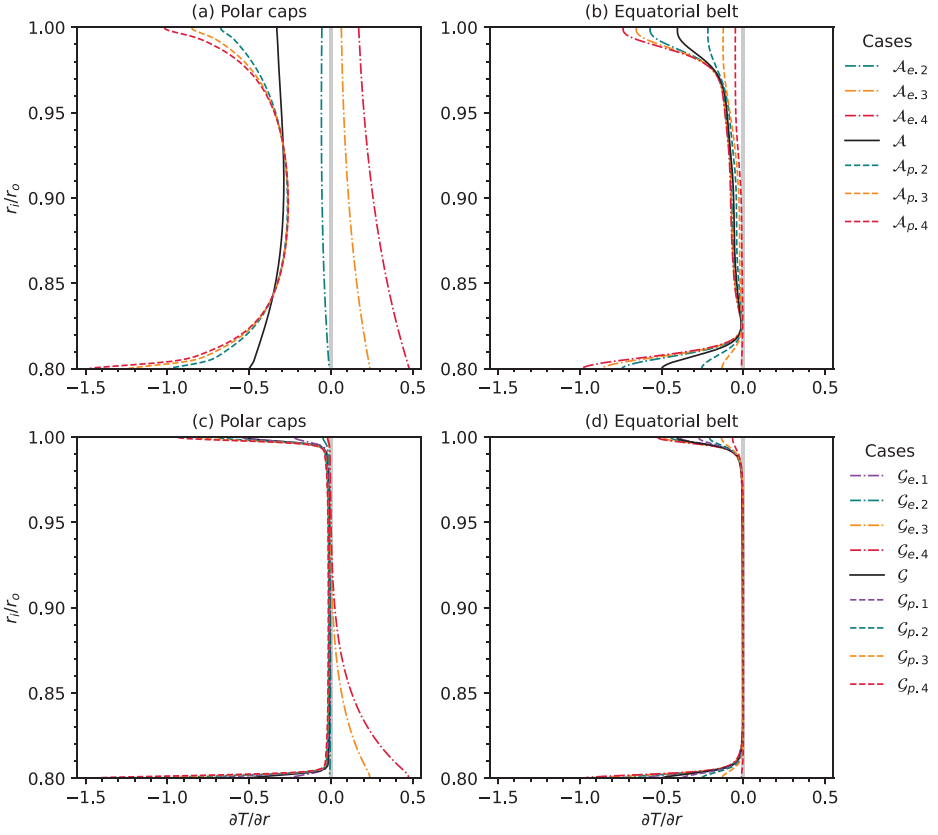

Fig. 9. Time-averaged radial profiles of $\partial T/\partial r$ for $\mathcal{A}$ (a and b) and $\mathcal{G}$ (c and d) models. Polar values were obtained by averaging over 5° from the geographic poles (a and c), equatorial values were obtained by averaging between latitudes 5° north to 5° south (b and d).

than radial temperature gradients hence may block or deflect convection rising from the bottom of the ocean. Based on models of phase transitions (Labrosse et al., 2018), Kvorka and Čadek (2024) introduced a numerical procedure to consistently link the ocean flow with the melting temperature variations arising from the deformation of the ice-water phase boundary at the top of the ocean. They used this coupled model to explore the formation of the ice-water interface topography. They found that the additional heat flux generated by variations in the melting temperature along the phase boundary counteracts the heat flux at the top of ocean but does not completely suppress it, with more heat flux reduction at high latitudes than near the equator (Kvorka and Čadek, 2024). However, in their approach the parameter controlling

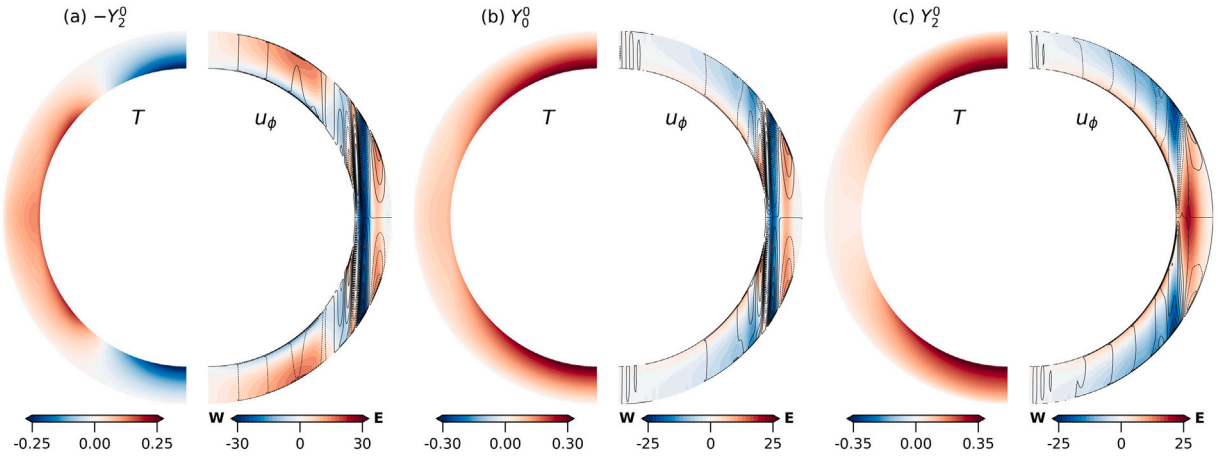

Fig. 10. Time-averaged zonal non-dimensional temperature (left) and non-dimensional velocity (right) for models $\mathcal{A}_{e.4}$ (a), $\mathcal{A}$ (b) and $\mathcal{A}_{p.4}$ (c). Solid/dashed contours denote anti-clockwise/clockwise meridional circulation, respectively. The temperature scale is expressed in terms of the temperature gradient at the bottom boundary by $\frac{\partial T}{\partial r}(r_i)D$, the velocity scale is expressed in units of $\frac{\nu}{D}$.

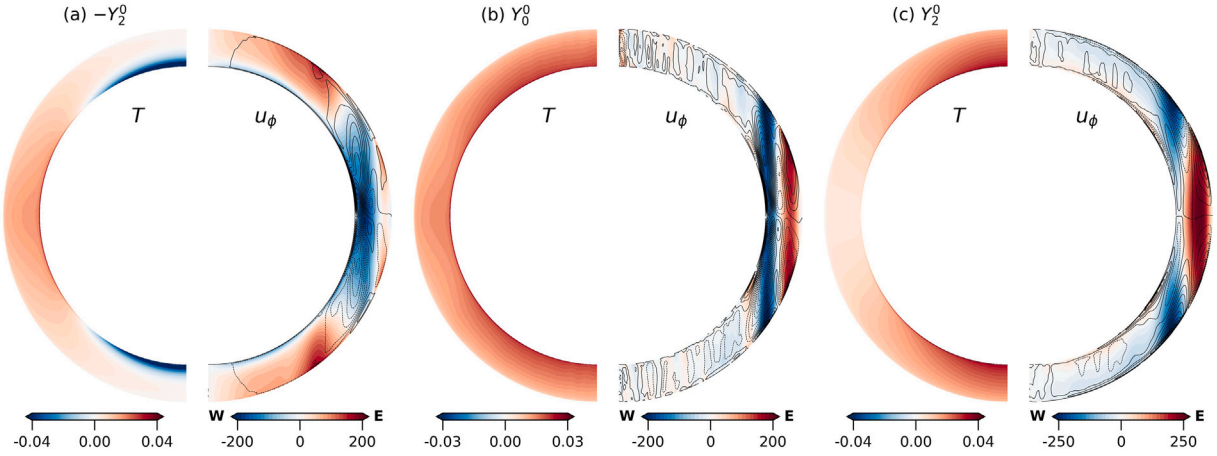

Fig. 11. As in Fig. 10 for models $\mathcal{G}_{e.4}$ (a), $\mathcal{G}$ (b) and $\mathcal{G}_{p.4}$ (c).

the water-ice interface temperature gradient is held fixed thus the strength of melting-temperature forcing relative to convective forcing might not be scaled properly when extrapolated.

Using different evolutions of phase boundary conditions that account for the topography driven relative strength of horizontal temperature differences, Gastine and Favier (2025) also studied the interplay between rotating convection and a melting boundary. They found that as with monophasic hydrodynamical models (e.g. Hartmann et al., 2024), the impact of rotation on the ocean flow determines the latitudinal heat flux pattern at the top of the ocean with a Rossby number delimiting the latitudinal dependence of overlying ice thinning in their models: thinner ice outside the TC is obtained for small Rossby number, thinner ice inside the TC is obtained for intermediate and no latitudinal preference for large Rossby number. Nevertheless, for large topographic lateral variations, ocean flows dynamics are determined by the coupling of ice melting effects and the rotating convection (Gastine and Favier, 2025).

Other ingredients, here not accounted for, may affect the resulting top cooling patterns, for example the value of the Prandtl number as well as the mechanical boundary conditions (Kvorka and Čadek, 2022; Hartmann et al., 2024). In the ocean-ice liquid–solid interface no slip is a natural choice. However, at rapidly rotating systems the Ekman layer is extremely thin hence free slip conditions may be more appropriate (e.g. Aurnou et al., 2008; Evonuk and Glatzmaier, 2009; Kvorka and Čadek, 2022). Although there are some differences in the resulting cooling pattern depending on the choice of mechanical boundary conditions, especially for very large convective forcing on approach to the non-rotating dynamical regime, the results for both no slip and free slip are qualitatively similar, with equatorial cooling for low forcing and polar cooling for large forcing (Kvorka and Čadek, 2022).

Given these limitations, we focused on the impact of the choice of a fixed heat flux prescribed at the seafloor on the resulting cooling pattern at the ocean ceiling and compared it with the choice of a fixed bottom temperature. We first considered cases where a homogeneous heat flux condition is prescribed. As in the case of fixed seafloor temperature (Amit et al., 2020; Kvorka and Čadek, 2022), competing effects of rotation, buoyancy and inertia control a transition between equatorial cooling (lower convective supercriticality) and polar cooling (higher convective supercriticality) (Fig. 2). When rotation effects become negligible for large enough convective supercriticality, latitudinal dependence of the outer boundary heat flux vanishes. Considering the regime diagram of Gastine et al. (2016), several moons (Titan, Europa, Ganymede) are likely close to the limit between the transitional and non-rotating regimes while Enceladus may be in the transitional regime (see Fig. 1 of Cabanes et al., 2024). Our models are placed in the appropriate transitional regime, as in previous studies (e.g. Amit et al., 2020; Kvorka and Čadek, 2022). In the case of a prescribed seafloor heat flux, however, the amplitude of the obtained ocean ceiling heat flux heterogeneity is much milder than in the case of a prescribed temperature, especially for equatorial cooling.

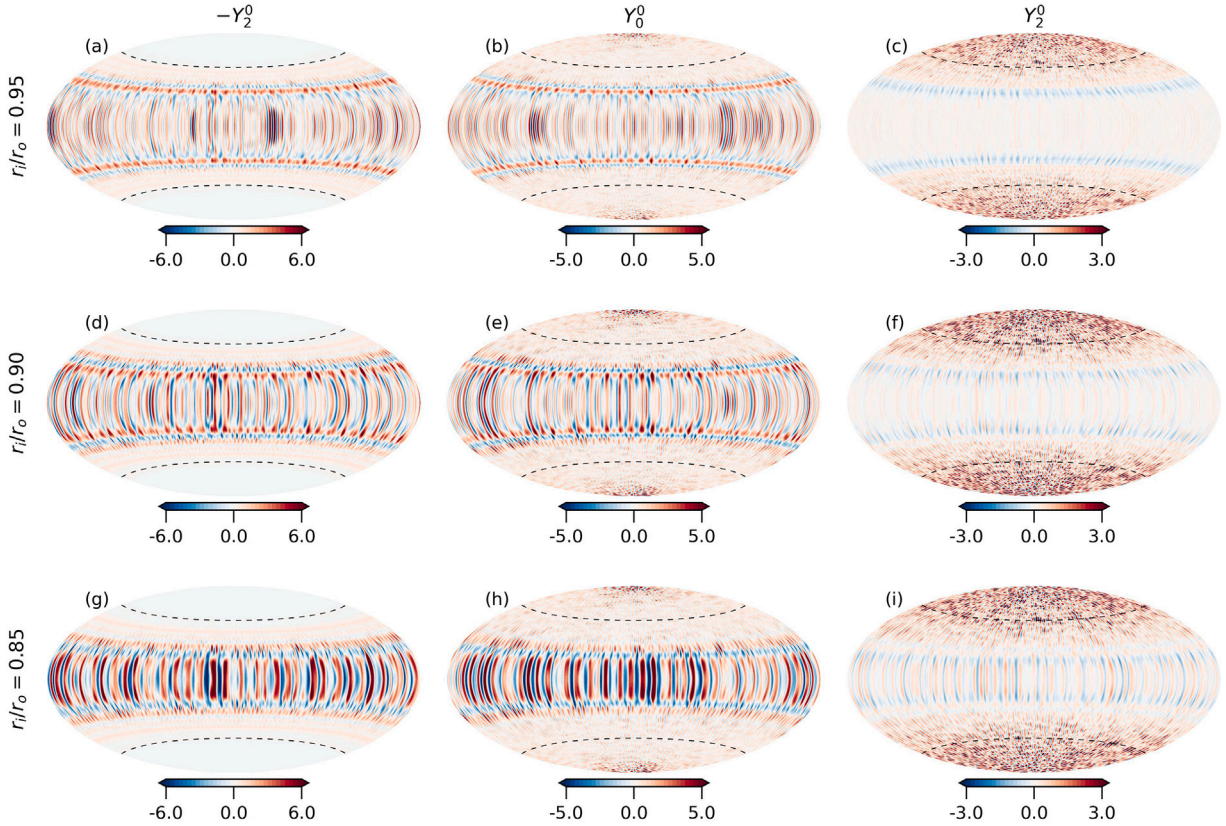

Fig. 12. Time-averaged radial non-dimensional velocity for models $\mathcal{A}_{e.4}$ (left column) with imposed inner boundary equatorial cooling heat flux and $q_i^* = 1.47$, $\mathcal{A}$ (middle column) with homogeneous conditions and $\mathcal{A}_{p.4}$ (right column) with imposed polar cooling and $q_i^* = 1.47$ at different radial levels from top to bottom: $r_i/r_o = 0.95$, 0.90 and 0.85, respectively. Dashed black lines denote the tangent cylinder. The velocity scale is expressed in units of $\frac{\nu}{D}$.

More importantly, we also investigated cases where a heterogeneous heat flux is prescribed at the seafloor and examined whether this bottom heat flux pattern is mirrored at the top of the ocean or whether the pattern emerging from rotational convection with a homogeneous flux prevails. The moderate amplitudes of bottom boundary heat flux heterogeneity prescribed in our models (Table 2) are in agreement with model predictions for the heat flux lateral variability at the seafloor of some icy moons, e.g. Titan (Choblet et al., 2017b) and Europa (Běhounková et al., 2021). For Enceladus, a significantly larger amplitude of inner boundary heterogeneity is predicted as a result of tidally-heating water circulation in a porous rocky core (Choblet et al., 2017a). Our results show that the location on the regime diagram only plays a secondary role on the cooling pattern. Indeed, when a large-scale heating heterogeneity with mild amplitude is present at the seafloor, the cooling pattern is systematically transposed to the ocean-ice interface regardless of the convective supercriticality (Fig. 6). However, the effectiveness of this transposition is likely to depend on the shell thickness, an effect that was not explored in this study.

While the amplitude of the heterogeneity imposed in our simulations is plausible and probably constitutes a lower end-member for ocean worlds such as Europa, Titan and Ganymede (Enceladus might be associated to a much stronger heterogeneity, see below), a legitimate question concerns the nature of the prescribed heat flux pattern. Plausible patterns can be illuminated by the dynamics of the solid layer beneath the ocean. In the case of Europa, for instance, simulations of thermal convection in the silicate mantle beneath the ocean indeed suggest a pattern where higher heat flux is expected at high latitudes (Běhounková et al., 2021). This is mostly related to the contribution of tidal heating in this rocky shell: while a minor part at the early stages of the moon's evolution where radiogenic heating prevails, tidal power may represent a significant fraction of the total heat at the seafloor in the last 2 Ga, even exceeding radiogenic decay during periods of elevated eccentricity.

Lemasquerier et al. (2023) imposed on their ocean model a bottom heat flux pattern inferred from the results of Běhounková et al. (2021). They found that the seafloor polar heating leads to polar cooling at the top of the ocean regardless of the cooling pattern in the reference homogeneous bottom heat flux case. Our results obtained for the synthetic idealized Y_2^0 heat flux pattern essentially confirm these findings. We note that the equatorial cooling in our reference homogeneous seafloor heat flux case is twice stronger than that of Lemasquerier et al. (2023) (compare our Fig. 4 with their Fig. 4c). Nevertheless, the bottom polar heating overcomes this stronger equatorial cooling in our reference homogeneous seafloor heat flux case to reverse the cooling pattern at the top of the ocean and yield strong polar cooling.

The distribution of heating in solid layers owing to tidal dissipation essentially reflects the structure of planetary interiors in terms of geometry and rheology. A compelling example is proposed in models dedicated to Jupiter's moon Io (cf. e.g. Segatz et al., 1988; Hamilton et al., 2013; Kervazo et al., 2022): as for Europa, maxima of tidal dissipation are expected at high latitudes in the case of a shallow asthenosphere with significant melt; the same models indicate however that maximum tidal dissipation will occur at low latitudes in the case of a deeper mantle with moderate amounts of melt. While Io is not an ocean world, its example demonstrates that at some point of their evolution, some ocean worlds may present such a configuration with maximum heat flux at low latitudes. In this case, the $-Y_2^0$ pattern used in half of our simulations would be more appropriate. Whether maxima occur at the poles or at the equator, our results show that for large-scale bottom heat flux patterns, the imposed amplitude of heterogeneity q_i^* is roughly translated to the outer boundary, i.e. $q_o^* \sim q_i^*$ (Fig. 8b) in agreement with the findings of Lemasquerier et al. (2023).

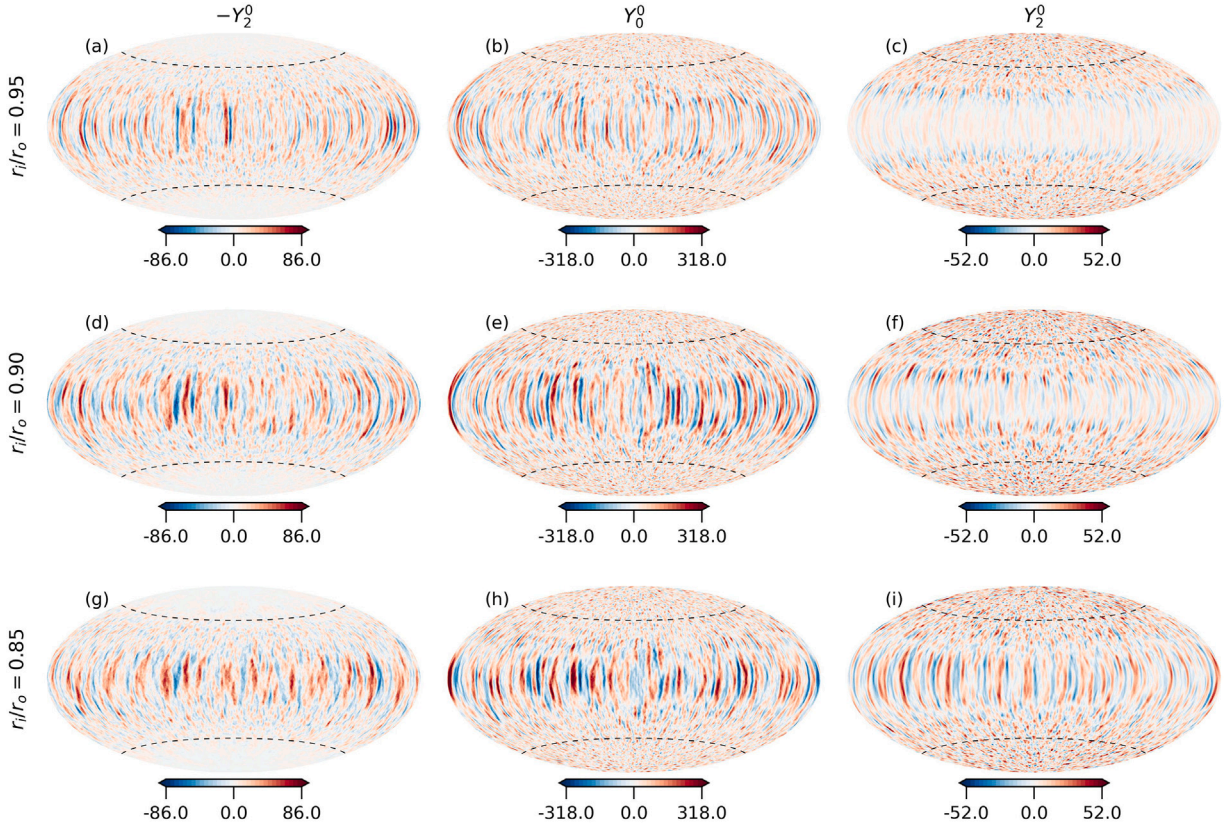

Fig. 13. As in Fig. 12 for models $\mathcal{G}_{e.4}$ (left column) with imposed inner boundary equatorial cooling heat flux and $q_i^* = 1.47$, $\mathcal{G}$ (middle column) with homogeneous condition and $\mathcal{G}_{p.4}$ (right column) with imposed polar cooling and $q_i^* = 1.47$.

While the tidal heating pattern might not be drastically altered by the occurrence of thermal convection in a solid shell (cf. e.g. Běhounková et al., 2010), other phenomena such as multiphasic flows may produce more pronounced distortions. In the case of Enceladus, for instance, tidal dissipation within a porous rocky core should involve maximal heating at high latitudes and along the leading and trailing meridians. Convection of interstitial water in the core modulates this pattern by focussing upward transport which yields a seafloor pattern with a single narrow band of high heat flux constituting mainly a great circle composed of the two meridians mentioned above (Choblet et al., 2017a). Overall, polar heating of the seafloor prevails. In a similar framework, if an inner fraction of this unconsolidated rocky core has a reduced porosity owing for instance to a larger gravity (as could be expected for Enceladus' neighbor Dione) equatorial heating prevails (Kervazo et al., 2019).

Bouffard et al. (2025) proposed ocean circulation models for Enceladus that showed that the polar heating pattern translates into strong polar cooling at the top of Enceladus' ocean which explains the polar thinning of the ice crust (Čadek et al., 2019) and south pole activity (Porco et al., 2006; Spencer et al., 2006; Howett et al., 2011). The same simulations indicate, however, that due to their narrow width, the meridional bands are smoothed out at low latitudes by strong zonal flows which results overall in a less effective translation of the heterogeneity amplitude to the outer boundary.

The length scale of the seafloor heat flux heterogeneity may indeed play an important role. In the cases of Titan and Ganymede, solid-state convection in the high pressure ice mantle beneath the ocean results in a much smaller scale seafloor heat flux pattern without any clear latitudinal dependence (Choblet et al., 2017b). Imposing such a pattern on rotating convection simulations in a thin spherical shell only slightly affects the level of equatorial or polar cooling (Terra-Nova et al., 2023). In such cases, the cooling pattern at the ocean/ice crust interface will be determined by the competition between rotation and convection in the ocean (Soderlund, 2019; Amit et al., 2020; Kvorka and Čadek, 2022). However, as for the homogeneous models of this study, the models of Terra-Nova et al. (2023) present milder magnitude of the equatorial vs. polar cooling ratio than models with fixed bottom temperature (Fig. 2).

Furthermore, the specific cases of the largest icy moons (Ganymede, Titan, Callisto) involve a secondary phase change for water: besides the top ice/ocean interface, the bottom boundary consists in a phase change from liquid ocean water to high pressure ice polymorphs in the solid layer below. A correct treatment of this specific interface implies a dedicated modeling, as noted earlier (cf. Section 1) for the ice crust/ocean interface (cf. e.g. Labrosse et al., 2018; Kvorka and Čadek, 2024). From the solid side, Lebec et al. (2023) implemented such a boundary condition that can be compared to models assuming an impermeable boundary (Choblet et al., 2017b; Kalousová et al., 2018). From the liquid side, it can be anticipated that models with a prescribed bottom temperature (i.e. the melting point) are certainly closer to reality than models with a prescribed flux (as is the case in the present study). A more realistic boundary condition nevertheless remains to be designed.

5. Conclusions

We have investigated the effect of prescribing a fixed heat flux pattern at the bottom of the ocean in an icy world. Below we enlist our main findings.

First, in case of a homogeneous pattern, we demonstrated that, owing to a competition between inertia, buoyancy and rotation, the resulting heat flux pattern at the ocean ceiling undergoes a transition upon increasing the convective supercriticality: either equatorial cooling (lower supercriticality) or polar cooling (higher supercriticality)

are obtained. These results resemble what was previously obtained for ocean convection simulations with a prescribed basal temperature (e.g. Soderlund et al., 2014; Amit et al., 2020; Kvorka and Čadek, 2022; Hartmann et al., 2024), albeit with a less pronounced equatorial cooling.

Second, when a heterogeneous large scale ($\pm Y_2^0$) heat flux pattern is prescribed at the seafloor, it is transmitted to the ocean ceiling even for low values ($q_i^* \sim 0.37$) of the pattern heterogeneity, whatever the intrinsic pattern that would be developed by rotational convection for a homogeneous heat flux. Note that for $q_i^* < 1$ convection is supercritical everywhere at the top of the shell and no local stratification develops. Previous studies of rotating convection with Earth's core thick shell geometry attempted to find the critical amplitude of boundary heterogeneity that allows penetration across the entire shell. Results from laboratory experiments suggest that global locking of the convection to the imposed outer boundary heat flux pattern is obtained for $q_i^* > 0.7$ (Sumita and Olson, 1999, 2002). Numerical dynamo simulations demonstrated that a boundary-driven thermal anomaly at the top of Earth's outer core may explain the lateral seismic heterogeneity at the top of the inner core (Aubert et al., 2008; Gubbins et al., 2011). In contrast, extrapolation of results from non-magnetic numerical simulations to Earth's core conditions suggest the boundary-driven thermal anomaly at the core-mantle boundary does not penetrate all the way to the inner-core boundary (Davies and Mound, 2019). Obviously, penetration of convection across a thin layer as in the case of subsurface oceans of icy moons is much more attainable than in Earth's thick outer core. According to Fig. 7 the boundary-driven convection determines the pattern of cooling from heterogeneity amplitudes as low as $q_i^* \approx 0.1$. Solid convection models for the envelopes beneath the oceans of icy moons suggest $q_i^* \approx 0.2$ for Europa (Běhounková et al., 2021; Lemasquerier et al., 2023) while in the case of Enceladus the concentrated bottom boundary pattern may lead to $q_i^* \approx 10 - 30$ (Choblet et al., 2017a; Bouffard et al., 2025), hence in both cases boundary control is expected to overcome the background main convection effect. Ganymede and Titan are likely characterized by very small-scale bottom boundary heat flux patterns (Choblet et al., 2017b; Terra-Nova et al., 2023) for which our study is less applicable.

The dynamical signature of the latitude of the tangent cylinder is less pronounced with a $\pm Y_2^0$ pattern. The amplitude of the ocean-ice heat flux heterogeneity resembles the one prescribed at the seafloor except in the case of equatorial cooling because of possible stratification at high latitudes. In the case of polar cooling, our results essentially confirm those established by Lemasquerier et al. (2023) with a more complex pattern for Europa.

When applied to real ocean worlds in the outer Solar System, these results yield several important implications for the geophysical characterization of the ocean from spacecraft measurements. Such studies have been proposed from past missions (Galileo and Cassini-Huygens) and constitute essential goals for ongoing missions (Juice and Europa Clipper) as well as mission projects dedicated to Enceladus. This typically involves two independent approaches (cf. e.g. for the Juice mission, Van Hoolst et al., 2024): first, if the multi-frequency electromagnetic induction response of the ocean can be separated from other contributions, ocean thickness and conductivity can be determined. If velocities are sufficiently large, which may be the case for Ganymede as scrutinized by the Juice spacecraft, induction could even yield constraints on ocean dynamics as recently shown by Šachl et al. (2025) or Kvorka et al. (2026). Second, a combination of gravity and shape measurements also provides constraints on the structure of the hydrosphere. As for electromagnetic induction, average thicknesses of the various water layers can be constrained from observations of tidal deformation and rotation of the moons. Models of ice shell compensation and associated assumptions also enable to compute ice shell thickness variations: as warm ice above the ice/ocean interface has a moderate viscosity, topography of this interface is expected to relax on short time scales so that persisting undulations can be interpreted in terms of heat flux variations (cf. e.g. Čadek et al., 2017; Kihoulou et al., 2023).

Table 3 summarizes how such inferences from spacecraft measurements shall be interpreted in the light of results from the present study. We note that only the central panels (Table 3c, d) refer to the simulations performed for this study, while other panels (Table 3a, b, e, f) arise from comparison with previous works.

Third, in the case of the largest ocean worlds such as Ganymede and maybe Titan, it is expected that the seafloor might in fact be a phase boundary with a high-pressure ice layer (Table 3a,b). Although further modeling work needs to be dedicated to such a case, this boundary resembles more one where the melting temperature is prescribed than one where the heat flux is prescribed. For this reason, one should expect that the heat flux pattern at the bottom of the ice shell should emerge from the competition between convection and rotation in the ocean, as already proposed (e.g. Amit et al., 2020; Kvorka and Čadek, 2022). This reinforces the notion that the Juice mission will provide means to decipher with unprecedented details the structure of Ganymede's hydrosphere (Van Hoolst et al., 2024; Hussmann et al., 2025): monitoring the ice shell structure should shed light on the ocean dynamics with a possible independent assessment from electromagnetic induction. Furthermore, establishing models of latitudinal profiles for the ice/ocean heat flux may potentially include information about the latitude of the tangent cylinder thus providing further means to constrain the structure of the hydrosphere. Conversely, this also implies that details on the distribution of heat in the deeper interior (rock mantle, metallic core) might not induce a clear signature in the present day structure of the ice shell.

Fourth, for intermediate sized moons such as Europa, a direct contact is expected between the ocean and the rocky mantle (Table 3c, d). The most appropriate bottom boundary condition for heat transfer is then a prescribed heat flux. Latitudinal heterogeneity at Europa's seafloor depends on the strength of tidal dissipation relative to radiogenic heating (Běhounková et al., 2021). During periods of low eccentricity/weakly dissipative mantle, the seafloor heat flux should be dominated by radiogenic power resulting in a rather homogeneous heat flux pattern. The heat flux at the ocean ceiling would be controlled by the ocean dynamics, thus resulting in equatorial cooling. During periods of enhanced eccentricity/strongly dissipative mantle, higher heat flux is expected in the polar regions (Běhounková et al., 2021). As shown by Lemasquerier et al. (2023), for such a pattern at the seafloor with maxima under the poles, it should be expected that the pattern is transmitted at the ocean ceiling (Table 3d). At present, it is still unclear what is the strength of tidal dissipation in Europa's mantle. Latitudinal variations of ice shell thickness determined by combined magnetic induction, altimetric, gravimetric and radar techniques by Europa Clipper (Roberts et al., 2023) will be essential to determine the appropriate heat regime for Europa at present and provide some constraints on the heat flux at the seafloor.

Fifth, for even smaller moons, such as Saturn's mid-sized inner moons (Enceladus, Mimas, and maybe Dione), it is possible that the rocky core is not consolidated (Table 3e, f). Choblet et al. (2017a) proposed that in this case, tidal power in the porous core could be significant and that a dissipation pattern with mild heterogeneity might be drastically altered by convection of interstitial water. In this case, seafloor heat flux is even more heterogeneous and maxima are possibly restricted to narrow bands. Bouffard et al. (2025) showed that for such a pattern (distinct from the large-scale pattern used here), polar heating of the ocean at the seafloor still induces polar cooling of the ocean at the interface between the ocean and the ice crust, as observed in our framework. However, narrow low latitude high flux features (not present in our framework) are likely smoothed out by powerful zonal winds outside the tangent cylinder. For this reason, in this specific case, inferring the heat flux from the ocean to the ice shell would superpose a deep seafloor signal at high latitudes and a possible manifestation of the tangent cylinder as a transition with regions at low

Table 3
Schematic illustrations of the possible impact of heterogeneous seafloor heat flux on ocean dynamics and surface ice thickness. Black and white vertical arrows denote respectively heat fluxes through the ocean ceiling and seafloor, with length indicating larger or smaller flux. White vertical dashed boundaries denote the latitude of the tangent cylinder. Φ means porosity, i.e. the amout of partial melting in the case of magmatism.

moon type	large		medium		small	
example	Ganymede/Titan?		Europa		Dione?	Enceladus
ocean ceiling cooling pattern	equatorial	polar	equatorial	polar	equatorial?	polar
origin	ocean dynamics		deeper heat		deeper heat and ocean dynamics	
obs. constraint	hydrosphere structure and ocean flow		ocean flow	deep thermal history	thermal history and ocean flow	
	a)	b)	c)	d)	e)	f)
	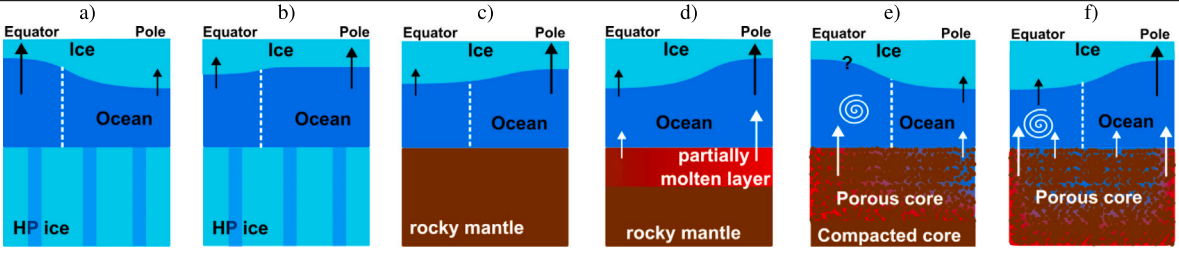					
seafloor BC	prescribed temperature? (phase change)		prescribed flux (large scale)		prescribed flux (narrow bands)	
origin	–	–	radiogenic heat with only weak heterogeneity	asthenosphere with significant melt fraction	porous core with compacted inner core	porous core

latitudes where lateral heterogeneity vanishes. Furthermore, monitoring the time-variable magnetic field environment of such ocean worlds could help constraining their interiors including the porous core and the likelihood of an inner core with reduced permeability, as already suggested from Cassini measurements at Enceladus (Saur et al., 2024).

The focus of this study is the impact of heterogeneous bottom heating patterns on the resulting cooling patterns at the top of the ocean. Thus, the imposed pattern at the bottom of the spherical shell is the main ingredient that has been explored in the setup of the numerical models. The control parameters of the simulations are very far from realistic conditions, in particular the Ekman number is way too large. Numerical simulations with lower Ekman numbers are computationally very costly. Further decreasing the Ekman number with different patterns of boundary conditions would require very long runs in order to properly converge towards patterns that are statistically representative of the heterogeneous boundary conditions. However, the rotating convection dynamics depends not only on the Ekman number but rather on a combination of all control parameters which is captured by an effective Rossby number (Gastine et al., 2016; Amit et al., 2020; Kvorka and Čadek, 2022, 2024). Indeed, decreasing the Ekman number while adjusting the other control parameters to maintain the same effective Rossby number yields practically identical convection patterns (Kvorka and Čadek, 2024). The same holds for the magnetohydrodynamics in the context of Earth's liquid outer core — decreasing the Ekman number while keeping all other control parameters fixed might actually lead to less Earth-like simulated magnetic fields (Christensen et al., 2010) hence the right way to approach Earth-like conditions is to follow a specific path in parameters space (Aubert et al., 2017). Furthermore, in particular to models driven by large-scale boundary heterogeneity, the dynamics is expected to be independent of viscous and small-scale inertial effects (Aubert et al., 2017; Aubert, 2019; Davies and Mound, 2019; Biggin et al., 2026). Nevertheless, to verify the robustness of our results in particular concerning the mixing properties, extension of this work to lower Ekman numbers will be explored in a future study.

CRediT authorship contribution statement

Filipe Terra-Nova: Writing – review & editing, Writing – original draft, Visualization, Software, Methodology, Investigation, Formal analysis, Data curation, Conceptualization. **Hagay Amit:** Writing – review & editing, Validation, Conceptualization. **Gaël Choblet:** Writing – review & editing, Project administration, Investigation, Conceptualization. **Mathieu Bouffard:** Writing – review & editing, Investigation, Formal analysis. **Gabriel Tobie:** Writing – review & editing, Validation, Investigation. **Ondřej Čadek:** Writing – review & editing, Validation.

Declaration of competing interest

The authors declare that they have no known competing financial interests or personal relationships that could have appeared to influence the work reported in this paper.

Acknowledgments

We thank Dr. Mathilde Kervazo for fruitful discussions. This study acknowledges the financial support from the French Agence Nationale de Recherche (ANR), France, project COLOSSE, France (ANR-2020-CE49-0010). F.T.-N. was supported by the Centre National d'Études Spatiales (CNES), France under the project MIMES. H.A. acknowledges ANR DYRE-COMB (grant ANR-22-CE49-0016–01). M.B. was supported by ERC PROMISES, France, project #101054470. O.Č. was supported by the Czech Science Foundation, Czechia, project No. 25-16801S. We thank Guy Moebs for his help in setting up the MagIC dynamo code (https://github.com/magic-sph/magic) on the GLICID (le Groupement Ligérien pour le Calcul Intensif Distribué) computational center where the numerical simulations for this study were performed.

Data availability

Data will be made available on request.

References

Ames, F., Ferreira, D., Czaja, A., Masters, A., 2025. Ocean stratification impedes particulate transport to the plumes of enceladus. Commun. Earth & Environ. 6 (1), 63.

Amit, H., Choblet, G., Olson, P., Monteux, J., Deschamps, F., Langlais, B., Tobie, G., 2015. Towards more realistic core-mantle boundary heat flux patterns: A source of diversity in planetary dynamos. Prog. Earth Planet. Sci. 2, 26. http://dx.doi.org/10.1186/s40645-015-0056-3.

Amit, H., Choblet, G., Tobie, G., Terra-Nova, F., Čadek, O., Bouffard, M., 2020. Cooling patterns in rotating thin spherical shells – application to titan's subsurface ocean. Icarus 338, 113509.

Ashkenazy, Y., Tziperman, E., 2021. Dynamic europa ocean shows transient taylor columns and convection driven by ice melting and salinity. Nat. Commun. 12 (1), 6376.

Aubert, J., 2019. Approaching Earth's core conditions in high resolution geodynamo simulations. Geophys. J. Int. 219 (S1), S137–S151.

Aubert, J., Amit, H., Hulot, G., Olson, P., 2008. Thermo-chemical wind flows couple Earth's inner core growth to mantle heterogeneity. Nature 454, 758–761.

Aubert, J., Gastine, T., Fournier, A., 2017. Spherical convective dynamos in the rapidly rotating asymptotic regime. J. Fluid. Mech. 813, 558–593.

Aurnou, J., Andreadis, S., Zhu, L., Olson, P., 2003. Experiments on convection in Earth's core tangent cylinder. Earth Planet. Sci. Lett. 212, 119–134.

Aurnou, J., Heimpel, M., Allem, L., King, E., Wicht, J., 2008. Convective heat transfer and the pattern of thermal emission on the gas giants. Geophys. J. Int. 173, 793–801.

Aurnou, J.M., Horn, S., Julien, K., 2020. Connections between nonrotating, slowly rotating, and rapidly rotating turbulent convection transport scalings. Phys. Rev. Res. 2, 043115.

Běhounková, M., Tobie, G., Choblet, G., Čadek, O., 2010. Coupling mantle convection and tidal dissipation: Applications to enceladus and Earth-like planets. J. Geophys. Res. 115, E09011.

Běhounková, M., Tobie, G., Choblet, G., Kervazo, M., Daswani, M.M., Dumoulin, C., Vance, S.D., 2021. Tidally induced magmatic pulses on the oceanic floor of jupiter's moon europa. Geophys. Res. Lett. 48, e2020GL090077.

Biggin, A., Davies, C., Mound, J., et al., 2026. Mantle heterogeneity influenced Earth's ancient magnetic field. Nat. Geosci. 19, 345–352.

Bire, S., Kang, W., Ramadhan, A., Campin, J.-M., Marshall, J., 2022. Exploring ocean circulation on icy moons heated from below. J. Geophys. Res. 127 (3), e2021JE007025.

Bire, S., Mittal, T., Kang, W., Ramadhan, A., Tuckman, P.J., German, C.R., Thurnherr, A.M., Marshall, J., 2023. Divergent behavior of hydrothermal plumes in fresh versus salty icy ocean worlds. J. Geophys. Res.: Planets 128 (11), e2023JE007740.

Bouffard, M., Choblet, G., Amit, H., Tobie, G., Čadek, O., Terra-Nova, F., 2025. Seafloor hydrothermal control over ocean dynamics in enceladus. Nat. Astron. 1–8.

Busse, F.H., 1975. A model of the geodynamo. Geophys. J. R. Astron. Soc. 42, 437–459.

Cabanes, S., Gastine, T., Fournier, A., 2024. Zonostrophic turbulence in the subsurface oceans of the jovian and saturnian moons. Icarus 415, 116047.

Čadek, O., Běhounková, M., Tobie, G., Choblet, G., 2017. Viscoelastic relaxation of Enceladus's ice shell. Icarus 291, 31–35.

Čadek, O., Souček, O., Běhounková, M., Choblet, G., Tobie, G., Hron, J., 2019. Long-term stability of Enceladus uneven ice shell. Icarus 310, 476–484.

Choblet, G., Tobie, G., Sotin, C., Běhounková, M., Čadek, O., Postberg, F., Souček, O., 2017a. Powering prolonged hydrothermal activity inside enceladus. Nat. Astro. 1 (12), 841.

Choblet, G., Tobie, G., Sotin, C., Kalousova, K., Grasset, O., 2017b. Heat transport in the high-pressure ice mantle of large icy moons. Icarus 285, 252–262.

Christensen, U.R., Aubert, J., Hulot, G., 2010. Conditions for Earth-like geodynamo models. Earth Planet. Sci. Lett. 296, 487–496.

Christensen, U.R., Olson, P., 2003. Secular variation in numerical geodynamo models with lateral variations of boundary heat flow. Phys. Earth Planet. Inter. 138, 39–54.

Davies, C., Mound, J., 2019. Mantle-induced temperature anomalies do not reach the inner core boundary. Geophys. J. Int. 219, S21–S32.

Dziewonski, A.M., Anderson, D.L., 1981. Preliminary reference earth model. Phys. Earth Planet. Inter. 25 (4), 297–356.

Evonuk, M., Glatzmaier, G.A., 2009. The effects of rotation rate on deep convection in giant planets with small solid cores. Planet. Space Sci. 55, 407–412.

Frasson, T., Schaeffer, N., Nataf, H.-C., Labrosse, S., 2025. Geomagnetic dipole stability and zonal flow changes controlled by mantle heat flux heterogeneities. Geophys. J. Int. 240 (3), 1481–1504.

Gastine, T., Aurnou, J.M., 2023. Latitudinal regionalization of rotating spherical shell convection. J. Fluid Mech. 954, R1.

Gastine, T., Favier, B., 2025. Rotating convection with a melting boundary: an application to the icy moons. Icarus 389, 116441.

Gastine, T., Wicht, J., Aubert, J., 2016. Scaling regimes in spherical shell rotating convection. J. Fluid Mech. 808, 690–732.

Gastine, T., Wicht, J., Aurnou, J.M., 2015. Turbulent Rayleigh–Bénard convection in spherical shells. J. Fluid Mech. 778, 721–764.

Glatzmaier, G., Coe, R., Hongre, L., Roberts, P., 1999. The role of the Earth's mantle in controlling the frequency of geomagnetic reversals. Nature 401, 885–890.

Gubbins, D., Sreenivasan, B., Mound, J., Rost, S., 2011. Melting of the Earth's inner core. Nature 473, 361–363.

Gubbins, D., Willis, P.W., Sreenivasan, B., 2007. Correlation of Earth's magnetic field with lower mantle thermal and seismic structure. Phys. Earth Planet. Inter. 162, 256–260.

Hamilton, C., Beggan, C., Still, S., Beuthe, M., Lopes, R., Williams, D., Radebaugh, J., Wright, W., 2013. Spatial distribution of volcanoes on Io: Implications for tidal heating and magma ascent. Earth Planet. Sci. Lett. 361, 272–286.

Hartmann, R., Stevens, R.J.A.M., Lohse, D., Verzicco, R., 2024. Toward understanding polar heat transport enhancement in subglacial oceans on icy moons. Geophys. Res. Lett. 51 (3), e2023GL105401.

Heimpel, M.H., Evans, M.E., 2013. Testing the geomagnetic dipole and reversing dynamo models over Earth's cooling history. Phys. Earth Planet. Inter. 224, 124–131.

Hemingway, D.J., Mittal, T., 2019. Enceladus's ice shell structure as a window on internal heat production. Icarus 332, 111–131.

Howett, C.J.A., Spencer, J.R., Pearl, J., Segura, M., 2011. High heat flow from enceladus' south polar region measured using 10-600 cm-1 Cassini/CIRS data. J. Geophys. Res. Atmos. 116, 189.

Hussmann, H., Lingenauber, K., Stark, A., Enya, K., Thomas, N., Lara, L.M., Althaus, C., Araki, H., Behnke, T., Binger, J., et al., 2025. The ganymede laser altimeter (gala) on the Jupiter icy moons explorer (juice) mission. Space Sci. Rev. 221 (3), 33.

Jansen, M., Kang, W., Kite, E., Zeng, Y., 2023. Energetics govern ocean circulation on icy ocean worlds. Planet. Sci. J. 4 (6), 117.

Jara-Orué, H., Vermeersen, B., 2016. Tides on Jupiter's moon Ganymede and their relation to its internal structure. Geol. Mijnb. /Neth. J. Geosci. 95 (2), 191–201.

Kalousová, K., Sotin, C., Choblet, G., Tobie, G., Grasset, O., 2018. Two-phase convection in Ganymede's high-pressure ice layer—implications for its geological evolution. Icarus 299, 133–147.

Kang, W., 2022. Different ice shell geometries on Europa and Enceladus due to their different sizes: Impacts of ocean heat transport. Astrophys. J. 934, 116.

Kang, W., 2023. The modulation effect of ice thickness variations on convection in icy ocean worlds. Mon. Not. R. Astron. Soc. 525 (4), 5251–5261.

Kang, W., Marshall, J., Mittal, T., Bire, S., 2022a. Ocean dynamics and tracer transport over the south pole geysers of Enceladus. Mon. Not. R. Astron. Soc. 517 (3), 3485–3494.

Kang, W., Mittal, T., Bire, S., Campin, J.-M., Marshall, J., 2022b. How does salinity shape ocean circulation and ice geometry on Enceladus and other icy satellites? Sci. Adv. 8 (29), eabm4665.

Kervazo, M., Choblet, G., Tobie, G., Sotin, C., Castillo-Rogez, J., 2019. Tidal dissipation in dione's porous rocky core: Implication for past geological activity and water-rock interactions. In: EPSC-DPS Joint Meeting 2019. 2019, pp. EPSC–DPS2019.

Kervazo, K., Tobie, G., Choblet, G., Dumoulin, C., Běhounková, M., 2022. Inferring Io's interior from tidal monitoring. Icarus 337, 114737.

Kihoulou, M., Čadek, O., Kvorka, J., Kalousová, K., Choblet, G., Tobie, G., 2023. Topographic response to ocean heat flux anomaly on the icy moons of Jupiter and Saturn. Icarus 381, 115337.

Kvorka, J., Čadek, O., 2022. A numerical model of convective heat transfer in Titan's subsurface ocean. Icarus 376, 114853.

Kvorka, J., Čadek, O., 2024. The role of subsurface ocean dynamics and phase transitions in forming the topography of icy moons. Icarus 412, 115985.

Kvorka, J., Čadek, O., Šachl, L., Velímský, J., 2026. Convective flow in Ganymede's subsurface ocean: Implications for the induced magnetic field and topography. Icarus 444, 116807.

Kvorka, J., Čadek, O., Tobie, G., Choblet, G., 2018. Does Titan's long-wavelength topography contain information about subsurface ocean dynamics? Icarus 310, 149–164.

Labrosse, S., Morison, A., Deguen, R., Alboussière, T., 2018. Rayleigh–Bénard convection in a creeping solid with melting and freezing at either or both its horizontal boundaries. J. Fluid. Mech. 846, 5–36.

Lebec, L., Labrosse, S., Morison, A., Tackley, P.J., 2023. Scaling of convection in high-pressure ice layers of large icy moons and implications for habitability. Icarus 396, 115494.

Lemasquerier, D.G., Bierson, C.J., Soderlund, K.M., 2023. Europa's ocean translates interior tidal heating patterns to the ice-ocean boundary. AGU Adv. 4 (6), e2023AV000994.

Lézin, M., Amit, H., Terra-Nova, F., Wardinski, I., 2023. Mantle-driven north-south dichotomy in geomagnetic polar minima. Phys. Earth Planet. Inter. 337, 107000.

Livermore, P., Hollerbach, R., Finlay, C., 2017. An accelerating high-latitude jet in Earth's core. Nat. Geosci. 10, 62–68.

Melosh, H., Ekholm, A., Showman, A., Lorenz, R., 2004. The temperature of Europa's subsurface water ocean. Icarus 168 (2), 498–502.

Mound, J., Davies, C., Rost, S., Aurnou, J., 2019. Regional stratification at the top of Earth's core due to core–mantle boundary heat flux variations. Nat. Geosci. 12, 575–580.

Nimmo, F., Pappalardo, R.T., 2016. Ocean worlds in the outer solar system. J. Geophys. Res.: Planets 121 (8), 1378–1399.

Nimmo, F., Thomas, P.C., Pappalardo, R.T., Moore, W.B., 2007. The global shape of Europa: Constraints on lateral shell thickness variations. Icarus 191 (1), 183–192.

Olson, P., Amit, H., 2014. Magnetic reversal frequency scaling in dynamos with thermochemical convection. Phys. Earth Planet. Inter. 229, 122–133.

Olson, P., Aurnou, J., 1999. A polar vortex in the Earth's core. Nature 402, 170–173.

Olson, P., Christensen, U.R., 2006. Dipole moment scaling for convection-driven planetary dynamos. Earth Planet. Sci. Lett. 250, 561–571.

Pedlosky, J., 1987. An inertial theory of the equatorial undercurrent. J. Phys. Oceanogr. 17 (11), 1978–1985.

Porco, C.C., Helfenstein, P., Thomas, P., Ingersoll, A., Wisdom, J., West, R., Neukum, G., Denk, T., Wagner, R., Roatsch, T., et al., 2006. Cassini observes the active south pole of enceladus. Science 311 (5766), 1393–1401.

Roberts, J.H., McKinnon, W.B., Elder, C.M., Tobie, G., Biersteker, J.B., Young, D., Park, R.S., Steinbrügge, G., Nimmo, F., Howell, S.M., et al., 2023. Exploring the interior of Europa with the Europa clipper. Space Sci. Rev. 219 (6), 46.

Šachl, L., Kvorka, J., Čadek, O., Velímský, J., 2025. Magnetic field induced by convective flow in Europa's subsurface ocean. Icarus 429, 116375.

Saur, J., Duling, S., Grayver, A., Szalay, J.R., 2024. Analysis of Enceladus's time-variable space environment to magnetically sound its interior. Planet. Sci. J. 5 (11), 245.

Schaeffer, N., 2013. Efficient spherical harmonic transforms aimed at pseudospectral numerical simulations. Geochem. Geophys. Geosyst. 14 (3), 751–758.

Segatz, M., Spohn, T., Ross, M.N., Schubert, G., 1988. Tidal dissipation, surface heat flow, and figure of viscoelastic models of Io. Icarus 75 (2), 187–206.

Soderlund, K.M., 2019. Ocean dynamics of outer solar system satellites. Geophys. Res. Lett. 46 (15), 8700–8710.

Soderlund, K., Schmidt, B., Wicht, J., Blankenship, D., 2014. Ocean-driven heating of Europa's icy shell at low latitudes. Nat. Geosci. 310, 16–19.

Spencer, J., Pearl, J., Segura, M., Flasar, F., Mamoutkine, A., Romani, P., Buratti, B., Hendrix, A., Spilker, L., Lopes, R., 2006. Cassini encounters enceladus: Background and the discovery of a south polar hot spot. Science 311 (5766), 1401–1405.

Sreenivasan, B., 2009. On dynamo action produced by boundary thermal coupling. Phys. Earth Planet. Inter. 177, 130–138.

Sukoriansky, S., Galperin, B., Dikovskaya, N., 2002. Universal spectrum of two-dimensional turbulence on a rotating sphere and some basic features of atmospheric circulation on giant planets. Phys. Rev. Lett. 89, 124501.

Sumita, I., Olson, P., 1999. Laboratory model for convection in Earth's core driven by a thermally heterogeneous mantle. Science 286, 1547–1549.

Sumita, I., Olson, P., 2002. Rotating thermal convection experiments in a hemispherical shell with heterogeneous boundary heat flux: Implications for the Earth's core. J. Geophys. Res. 107 (B8), 2169.

Terra-Nova, F., Amit, H., 2024. Regionally-triggered geomagnetic reversals. Sci. Rep. 14, 9639.

Terra-Nova, F., Amit, H., Choblet, G., Tobie nd, G., Čadek, O., 2023. The influence of heterogeneous seafloor heat flux on the cooling patterns of Ganymede's and Titan's subsurface oceans. Icarus 389, 115232.

Van Hoolst, T., Tobie, G., Vallat, C., Altobelli, N., Bruzzone, L., Cao, H., Dirkx, D., Genova, A., Hussmann, H., Iess, L., et al., 2024. Geophysical characterization of the interiors of Ganymede, callisto and europa by esa's Jupiter icy moons explorer. SSR 220 (5), 54.

Vance, S.D., Panning, M.P., Stähler, S., Cammarano, F., Bills, B.G., Tobie, G., Kamata, S., Kedar, S., Sotin, C., Pike, W.T., Lorenz, R., Huang, H.-H., Jackson, J.M., Banerdt, B., 2018. Geophysical investigations of habitability in ice-covered ocean worlds. J. Geophys. Res. : Planets 123 (1), 180–205.

Wicht, J., 2002. Inner-core conductivity in numerical dynamo simulations. Phys. Earth Planet. Inter. 132, 281–302.

Zeng, Y., Jansen, M.F., 2024. The effect of salinity on ocean circulation and ice–ocean interaction on enceladus. Planet. Sci. J. 5 (1), 13.

Zhang, Y., Kang, W., Marshall, J., 2024. Ocean weather systems on icy moons, with application to enceladus. Sci. Adv. 10, eadn6857.